

Many-Body Theory of Proton-Generated Point Defects for Losses of Electron Energy and Photons in Quantum Wells

Danhong Huang,¹ Andrii Iurov,² Fei Gao,³ Godfrey Gumbs,⁴ and D. A. Cardimona¹

¹*Air Force Research Laboratory, Space Vehicles Directorate, Kirtland Air Force Base, New Mexico 87117, USA*

²*Center for High Technology Materials, University of New Mexico, 1313 Goddard Street Southeast, Albuquerque, New Mexico 87106, USA*

³*Department of Nuclear Engineering and Radiological Sciences, University of Michigan, 500 South State Street, Ann Arbor, Michigan 48109, USA*

⁴*Department of Physics and Astronomy, Hunter College of the City University of New York, 695 Park Avenue, New York, New York 10065, USA*

 (Received 22 September 2017; revised manuscript received 6 December 2017; published 6 February 2018)

The effects of point defects on the loss of either energies of ballistic electron beams or incident photons are studied by using a many-body theory in a multi-quantum-well system. This theory includes the defect-induced vertex correction to a bare polarization function of electrons within the ladder approximation, and the intralayer and interlayer screening of defect-electron interactions is also taken into account in the random-phase approximation. The numerical results of defect effects on both energy-loss and optical-absorption spectra are presented and analyzed for various defect densities, numbers of quantum wells, and wave vectors. The diffusion-reaction equation is employed for calculating distributions of point defects in a layered structure. For completeness, the production rate for Frenkel-pair defects and their initial concentration are obtained based on atomic-level molecular-dynamics simulations. By combining the defect-effect, diffusion-reaction, and molecular-dynamics models with an available space-weather-forecast model, it will be possible in the future to enable specific designing for electronic and optoelectronic quantum devices that will be operated in space with radiation-hardening protection and, therefore, effectively extend the lifetime of these satellite onboard electronic and optoelectronic devices. Specifically, this theory can lead to a better characterization of quantum-well photodetectors not only for high quantum efficiency and low dark current density but also for radiation tolerance or mitigating the effects of the radiation.

DOI: [10.1103/PhysRevApplied.9.024002](https://doi.org/10.1103/PhysRevApplied.9.024002)

I. INTRODUCTION

Point defects (vacancies and interstitials) are produced by displacements of atoms from their thermal-equilibrium lattice sites [1,2], where the lattice-atom displacements are mainly caused by a proton-irradiation-induced primary knock on atom (PKA) on a time scale shorter than 100 ps for building up point defects without thermal reactions. These initial displacements are followed immediately by defect mutual recombinations or reactions with sinks (clustering or dissolution of clusters for point-defect stabilizations) [3,4] on a time scale shorter than 10 ns, then possibly by thermally activated defect migrations [5] up to a time scale much longer than 10 ns (steady-state distributions). Such atom displacements depend not only on the energy-dependent flux of protons but also on the differential energy transfer cross sections (probabilities) for collision between atoms, interatomic Coulomb interactions and even kinetic-energy loss to core-level electrons of an atom (ionizations). The sample temperature at which the irradiation is done also significantly affects the diffusion of

defects, their stability as clusters, and the formation of Frenkel pairs [6]. One of the effective calculation methods for studying the nonthermal spatiotemporal distributions of proton-irradiation-induced point defects is the molecular-dynamics (MD) model [7]. However, the system size increases quadratically with the initial kinetic energy of protons, and the time scale can easily run up to several hundred picoseconds. In this case, the defect reaction process driven by thermal migration cannot be included in the MD model due to its much longer time scale. Practically, if the system time evolution goes above 100 ps, either the kinetic lattice Monte Carlo [8] or the diffusion-reaction equation [9,10] method should be used instead.

In the presence of defects, dangling bonds attached to these point defects can capture Bloch electrons through multiphonon emission to form localized charge centers. The randomly distributed charge centers will further affect electron responses to either an external ballistic electron beam [11] or incident photons [12]. Physically, the defect modifications to the electron response function can be addressed by a vertex correction [12] to a bare electron

polarization function in the ladder approximation (LA) [13]. In addition, both the intralayer and interlayer screening corrections in a multi-quantum-well system can be included by using the random-phase approximation (RPA) [13,14]. The many-body theory presented here is crucial for understanding the full mechanism for characterizing defects [15] and defect effects [16], as well as for developing effective mitigation in early design stages of electronic devices. Equipped with this multi-time-scale microscopic theory [17], the experimental characterization of postirradiated test devices [18] is able to provide useful information on the device architecture's susceptibility to space radiation effects [19]. Furthermore, our physics model should also allow for the accurate prediction of device-performance degradation by using the space weather forecast [20,21] for a particular orbit. With this paper, we expect to bridge the gap between researchers studying radiation-induced damage in materials [1,2,22,23] and others characterizing irradiation-induced performance degradation in devices [24,25].

As for applications of the current theory, we would like to emphasize that space-based infrared (IR) imaging is expected to face the most stringent performance requirements on the quantum-well (QW) focal plane array (FPA) [26,27] due to the high payload cost, complexity, and remoteness the space environment imparts, as well as incident photon-flux levels occurring in space environments that are an order of magnitude or more lower than those found in terrestrial ones. Space applications also set up the unique requirement of radiation tolerance (or radiation hardness) on two elements of the hybridized QW FPA, i.e., the Si-CMOS readout integrated circuit and the photodetector array. FPAs developed for these purposes in a space environment are meticulously characterized for their sensitivity, uniformity, operability, and radiation hardness. IR detector arrays operated in the space environment are subjected to a variety of radiation sources while in orbit, e.g., electrons, protons, and some heavy ions confined by Earth's magnetic field (Van Allen radiation belts). This result indicates that QW photodetectors for space-based surveillance or space-situational awareness must be characterized in advance and should acquire not only high performance (high quantum efficiency and low dark current density) [28,29] but also radiation tolerance or an ability to withstand the effects of the radiation they would expect to encounter in a given orbit. Detector technologies that operate in the harsh radiation environment of space with better radiation tolerance would lead to greater flexibility in orbit selection, technical applications, and system sustainability and, therefore, are of more value to the space-based sensing community.

The rest of the paper is organized as follows. In Sec. II, we present our theoretical model and numerical results to highlight the defect effects on losses of electron energy and photons in multi-quantum-well systems, where defect potentials and vertex corrections, defect effects on partial and total polarization functions, electron-energy-loss

functions and intrasubband and intersubband absorption spectra have been demonstrated and analyzed. In Sec. III, ultrafast dynamics related to defect production, as well as the follow-up defect diffusion and reaction, are studied and a steady-state one-dimensional distribution function of point defects are calculated to provide a direct input for modeling the defect effects discussed in Sec. II. Finally, a summary and some remarks are presented in Sec. IV.

II. EFFECTS OF POINT DEFECTS

In this section, we first look into effects of point defects on the electron polarization function in a single wide quantum well. After generalizing the system to multiple quantum wells, we further study the kinetic-energy loss of a parallel (or perpendicular) electron beam. For comparison, we also calculate the loss of incident photons with a field polarization parallel (perpendicular) to the quantum-well planes, corresponding to intrasubband [30] (intersubband [31]) optical transitions of electrons.

A. Effects on electron polarization function

Since the wave functions of individual point defects are spatially localized, we expect that the interaction between electrons and charged point defects can only affect the screening to the intralayer Coulomb interaction. Therefore, we start with a study of defect effects in a single quantum well. The exchange-interaction-induced vertex correction to a bare polarization function of electrons in a quantum well has been addressed before [12] within the ladder approximation.

For an n -doped quantum well, the total electron polarization function [32] can be written as a sum of partial polarization functions, i.e., $\tilde{\chi}(q_{\parallel}, \omega) = \sum_{n \leq n'} \chi_{n,n'}(q_{\parallel}, \omega)$, where q_{\parallel} is an electron wave number, ω is the angular frequency of an electrical (or optical) perturbation, and $n \leq n' = 1, 2, \dots$ labels different energy subbands. Here, each partial polarization function $\chi_{n,n'}(q_{\parallel}, \omega)$ can be calculated through an inverse dielectric function $\mathcal{K}_{n,n';m,m'}(q_{\parallel}, \omega)$, according to [11]

$$\chi_{n,n'}(q_{\parallel}, \omega) = \sum_{m \leq m'} \mathcal{K}_{n,n';m,m'}(q_{\parallel}, \omega) \chi_{m,m'}^{(0)}(q_{\parallel}, \omega) \Gamma_{m,m'}(q_{\parallel}, \omega), \quad (1)$$

where $\Gamma_{m,m'}(q_{\parallel}, \omega)$ represents a defect-vertex correction, which is determined by Eq. (7) below, and the bare polarization function $\chi_{n,n'}^{(0)}(q_{\parallel}, \omega)$ takes the form

$$\begin{aligned} \chi_{m,m'}^{(0)}(q_{\parallel}, \omega) = & \frac{1}{2\pi^2} \int_0^{\infty} dk_{\parallel} k_{\parallel} \int_0^{2\pi} d\theta_{\mathbf{k}_{\parallel}, \mathbf{q}_{\parallel}} \\ & \times \left\{ \frac{f_0[\varepsilon_m(k_{\parallel})] - f_0[\varepsilon_{m'}(|\mathbf{k}_{\parallel} + \mathbf{q}_{\parallel}|)]}{\hbar\omega + i\gamma_0 - \varepsilon_{m'}(|\mathbf{k}_{\parallel} + \mathbf{q}_{\parallel}|) + \varepsilon_m(k_{\parallel})} \right. \\ & \left. + \frac{f_0[\varepsilon_{m'}(|\mathbf{k}_{\parallel} + \mathbf{q}_{\parallel}|)] - f_0[\varepsilon_m(k_{\parallel})]}{\hbar\omega + i\gamma_0 - \varepsilon_m(k_{\parallel}) + \varepsilon_{m'}(|\mathbf{k}_{\parallel} + \mathbf{q}_{\parallel}|)} \right\}. \quad (2) \end{aligned}$$

Here, $\theta_{\mathbf{k}_{\parallel}, \mathbf{q}_{\parallel}}$ is the angle between wave vectors \mathbf{k}_{\parallel} and \mathbf{q}_{\parallel} , γ_0 is the level broadening, $\varepsilon_n(k_{\parallel}) = \varepsilon_n + \hbar^2 k_{\parallel}^2 / 2\mu^*$ are subband energies, $\varepsilon_n = \pi^2 \hbar^2 n^2 / 2\mu^* L_W^2$, μ^* is the effective mass, L_W is the well width, $f_0(x) = \{1 + \exp[(x - u_c)/k_B T]\}^{-1}$ is the Fermi function, and u_c and T are the chemical potential and temperature of the electrons, respectively.

In addition, the inverse dielectric function $\mathcal{K}_{\ell, \ell', m, m'}(q_{\parallel}, \omega)$ in Eq. (1) satisfies

$$\sum_{m \leq m'} \mathcal{K}_{\ell, \ell', m, m'}(q_{\parallel}, \omega) \varepsilon_{m, m'; n, n'}(q_{\parallel}, \omega) = \delta_{\ell, n} \delta_{\ell', n'}, \quad (3)$$

where $\varepsilon_{m, m'; n, n'}(q_{\parallel}, \omega)$ is the dielectric function and can be calculated within the RPA [14] as (see the right panel of Fig. 1)

$$\varepsilon_{m, m'; n, n'}(q_{\parallel}, \omega) = \delta_{m, n} \delta_{m', n'} - \chi_{n, n'}^{(0)}(q_{\parallel}, \omega) \Gamma_{n, n'}(q_{\parallel}, \omega) \mathcal{V}_{m, m'; n, n'}(q_{\parallel}), \quad (4)$$

and the second term corresponds to the defect correction. In Eq. (4), $\mathcal{V}_{m, m'; n, n'}(q_{\parallel})$ represents the intralayer Coulomb matrix elements, given by [33]

$$\begin{aligned} \mathcal{V}_{m, m'; n, n'}(q_{\parallel}) &= \frac{e^2}{2\varepsilon_0 \varepsilon_d (q_{\parallel} + q_s)} \\ &\times \int dz \int dz' [\mathcal{F}_m(z)]^* \mathcal{F}_{m'}(z) e^{-q_{\parallel} |z - z'|} [\mathcal{F}_n(z')]^* \mathcal{F}_{n'}(z'), \end{aligned} \quad (5)$$

where ε_d is the host-material dielectric constant, $\mathcal{F}_n(z) = \sqrt{2/L_W} \sin[(n\pi/L_W)(z + L_W/2)]$ is the wave function of the n th subband, and

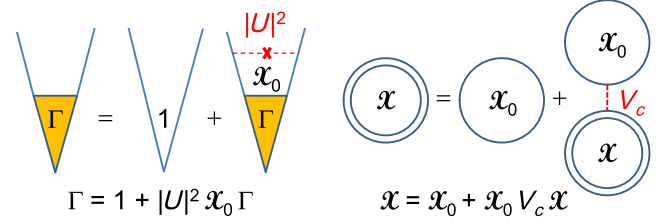


FIG. 1. (Left panel) Graphic representation for the ladder approximation used in Eq. (7). (Right panel) Graphic representation for the random-phase approximation employed in Eq. (21).

$$q_s = \frac{e^2}{2\pi\varepsilon_0 \varepsilon_d} \sum_n \int_0^\infty dk_{\parallel} k_{\parallel} \left(-\frac{\partial f_0[\varepsilon_n(k_{\parallel})]}{\partial \varepsilon_n(k_{\parallel})} \right), \quad (6)$$

which plays the role of the inverse of a static screening length [33]. The particle-in-a-box model for electrons in a quantum well not only is a reliable model for a number of existing realistic situations in semiconductor physics but also proves helpful for considering a simple mathematical model to reveal the details of an otherwise complicated theory for effects of defects. Furthermore, this model has been established to work satisfactorily for electrons in wide quantum wells with high-potential barriers and low electron densities for which tunneling is insignificant. Therefore, the overlap of electron wave functions in adjacent wells becomes negligible.

For the defect-vertex correction [12] $\Gamma_{n, n'}(q_{\parallel}, \omega)$ introduced in Eqs. (1) and (4), we find the following self-consistent equation within the LA (the left panel of Fig. 1):

$$\begin{aligned} \Gamma_{n, n'}(q_{\parallel}, \omega) &= 1 + \left(\frac{Z^* e^2}{2\varepsilon_0 \varepsilon_d} \right)^2 \frac{1}{2\pi^2} \int_0^\infty dp_{\parallel} p_{\parallel} \chi_{n, n'}^{(0)}(p_{\parallel}, \omega) \Gamma_{n, n'}(p_{\parallel}, \omega) \\ &\times \delta \left[\varepsilon_{n'} \left(\frac{q_{\parallel}}{2} \right) - \varepsilon_n \left(\frac{p_{\parallel}}{2} \right) \right] \int_{-\mathcal{L}_0/2}^{\mathcal{L}_0/2} dz_0 \rho_d(z_0) |U_{n, n'}(q_{\parallel}, p_{\parallel} | z_0)|^2 \\ &= 1 + \left(\frac{Z^* e^2}{2\varepsilon_0 \varepsilon_d} \right)^2 \frac{2\mu^*}{\pi^2 \hbar^2} \chi_{n, n'}^{(0)}(q_{\parallel}^*, \omega) \Gamma_{n, n'}(q_{\parallel}^*, \omega) \left(\int_{-\mathcal{L}_0/2}^{\mathcal{L}_0/2} dz_0 \rho_d(z_0) |\bar{U}_{n, n'}(q_{\parallel}, z_0)|^2 \right), \end{aligned} \quad (7)$$

where $q_{\parallel}^* = \sqrt{q_{\parallel}^2 + 8\mu^* \varepsilon_{n'n} / \hbar^2}$, $\varepsilon_{n'n} = \varepsilon_{n'} - \varepsilon_n \geq 0$, and the defect interaction with electrons $|\bar{U}_{n, n'}(q_{\parallel}, z_0)|^2 \equiv |U_{n, n'}(q_{\parallel}, q_{\parallel}^* | z_0)|^2$ is calculated as

$$|\bar{U}_{n, n'}(q_{\parallel}, z_0)|^2 = \int_0^\pi d\theta \left(\frac{e^{-\Delta_{n'n}^2(q_{\parallel}, \theta) \Lambda_{\parallel}^2 / 4}}{\Delta_{n'n}(q_{\parallel}, \theta) + q_s} \right)^2 \left(\int_0^{L_W/2} dz \mathcal{F}_n(z) \mathcal{F}_{n'}(z) [e^{-\Delta_{n'n}(q_{\parallel}, \theta) |z - z_0|} \pm e^{-\Delta_{n'n}(q_{\parallel}, \theta) |z + z_0|}] \right)^2, \quad (8)$$

the sign $+$ ($-$) corresponds to the case with $n = n' = 1$ or 2 ($n' = 2$ and $n = 1$), \mathcal{L}_0 is the system size, Z^* is the trapped charge number of a point defect, $2\Delta_{n'n}^2(q_{\parallel}, \theta) = q_{\parallel}^2 - q_{\parallel} \sqrt{q_{\parallel}^2 + 8\mu^* \varepsilon_{n'n} / \hbar^2} \cos \theta + 4\mu^* \varepsilon_{n'n} / \hbar^2$, Λ_{\parallel} is the correlation length for randomly distributed point defects, and $\rho_d(z_0)$ stands for the one-dimensional distribution function of point defects determined in Sec. III A. Here, $\int_{-\mathcal{L}_0/2}^{\mathcal{L}_0/2} dz_0 \rho_d(z_0) |\bar{U}_{1,2}(q_{\parallel}, z_0)|^2 = 0$ if $\rho_d(z_0) = \rho_d(-z_0)$.

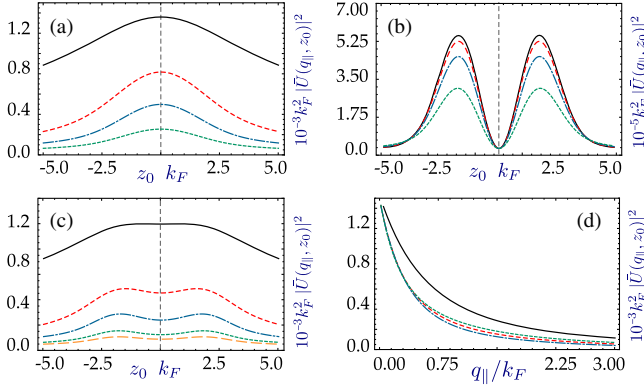


FIG. 2. $|U_{n,n'}(q_{||}, z_0)|^2$ (in units of k_F^{-2}) as functions of $z_0 k_F$ in (a) for $|\bar{U}_{1,1}|^2$ and $q_{||}/k_F = 0.1$ (black), 0.5 (red), 1.0 (blue), and 2.0 (green); in (b) for $|\bar{U}_{1,2}|^2$ and $q_{||}/k_F = 0.1$ (black), 1.0 (red), 2.0 (blue), and 3.0 (green); and in (c) for $|\bar{U}_{2,2}|^2$ and $q_{||}/k_F = 0.1$ (black), 0.5 (red), 1.0 (blue), 2.0 (green), and 3.0 (orange). (d) The same expression as a function of $q_{||}/k_F$ for $|\bar{U}_{1,1}|^2$, $k_F z_0 = 0.0$ (black) and 2.0 (red), and, for $|\bar{U}_{2,2}|^2$, $k_F z_0 = 0.0$ (blue) and 2.0 (green). Here, $k_F = \sqrt{2\pi n_{\text{QW}}}$ is the Fermi wave vector, $n_{\text{QW}} = 1.0 \times 10^{11} \text{ cm}^{-2}$ is the quantum-well doping density, $L_W = 100 \text{ nm}$, $\mu^* = 0.067 m_0$, with free-electron mass m_0 , and $\Lambda_{||} = 10 \text{ \AA}$.

The lowest-order approximate result of Eq. (7) can be obtained by simply replacing $\Gamma_{n,n'}(p_{||}, \omega)$ with 1 on the right-hand side of this equation. Therefore, the correction to $\Gamma_{n,n'}(q_{||}, \omega) \approx 1$ becomes proportional to the total number of point defects or the integral of $|\bar{U}_{n,n'}|^2$ with respect to z_0 . In general, the solution of Eq. (7) includes all of the higher orders of $|\bar{U}_{n,n'}|^2$ by going beyond the second-order Born approximation [34].

The results calculated from Eq. (8) for $|\bar{U}_{n,n'}(q_{||}, z_0)|^2$ are shown in Fig. 2, where the features in $|\bar{U}_{n,n}|^2$, with $n = 1, 2$, for the intrasubband interactions in Figs. 2(a) and 2(c) result from the symmetry and antisymmetry properties of the first two electron wave functions in a quantum well. On the other hand, $|\bar{U}_{1,2}|^2$ in Fig. 2(b) for intersubband interactions displays the overlap of these two electron wave functions with opposite symmetries, leading to two peaks and one node around $z_0 = 0$. From Figs. 2(a) and 2(c), we further find that both the peak strength and the peak width decrease with an increasing $q_{||}$, and the reduction of peak strength with $q_{||}$ can be seen more clearly from Fig. 2(d). In addition, a finite value of $\Delta_{21}(q_{||}, \theta)$ at $q_{||} = 0$ leads to a negligible $|\bar{U}_{1,2}|^2$ value, and, furthermore, the widths of the dual peaks in Fig. 2(b) spread out significantly with $q_{||}$.

Based on the calculated $|\bar{U}_{n,n'}(q_{||}, z_0)|^2$ value in Fig. 2, Eq. (7) can be applied to compute the dynamical defect-vertex correction $\Gamma_{n,n'}(q_{||}, \omega)$ with respect to unity in the ladder approximation. In order to simulate the physical distribution of defects shown in Fig. 9, we assume

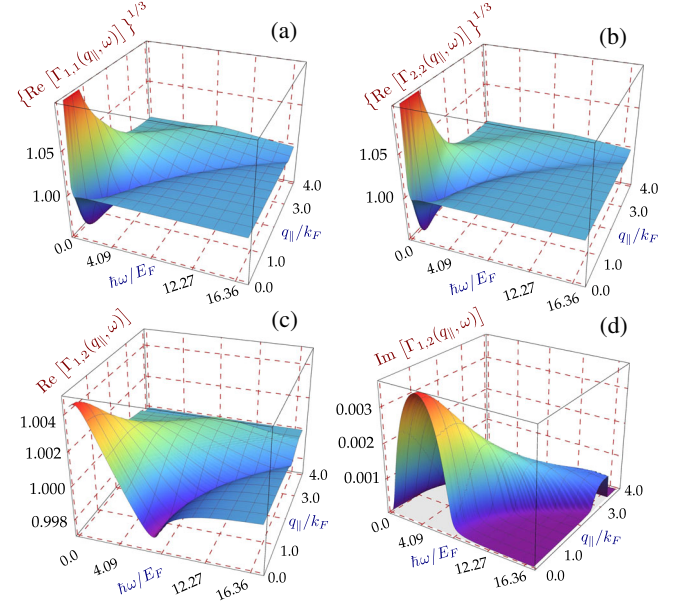


FIG. 3. 3D plots of a dimensionless $\Gamma_{n,n'}(q_{||}, \omega)$ value from the self-consistent solution of Eq. (7). Here, $Z^* = 1$, $T = 4 \text{ K}$, $E_F = \hbar^2 k_F^2 / 2\mu^*$, $\epsilon_d = 13.3$, $\mathcal{L}_0/L_W = 10$, $\rho_1 = 3.0 \times 10^6 \text{ cm}^{-1}$, $\rho_2 = 2.5 \times 10^6 \text{ cm}^{-1}$, $\rho_0 = 1.5 \times 10^6 \text{ cm}^{-1}$, $\Delta\rho = 1.0 \times 10^6 \text{ cm}^{-1}$, and $\kappa = 10$. The other parameters are the same as those in Fig. 2. Results for the real part of $\Gamma_{n,n'}(q_{||}, \omega)$ with $n = n' = 1$, $n = n' = 2$, and $n = 1, n' = 2$ are presented in (a), (b), and (c), respectively, while the result for the imaginary part of $\Gamma_{1,2}(q_{||}, \omega)$ is displayed in (d). Here, both subbands are occupied.

a regional form, i.e., $\rho_d(z_0)/\kappa = \rho_1 \Theta(-z_0 - L_W/2) + \rho_2 \Theta(z_0 - L_W/2) + [\rho_0 + z_0(\Delta\rho/L_W)] \Theta(L_W/2 - |z_0|)$, where $\Theta(x)$ is a unit-step function and κ is a scaling number. Similar dependences on both ω and $q_{||}$ are seen in Figs. 3(a) and 3(b), respectively, where a very strong intrasubband-scattering resonance associated with a sign switching in $\text{Re}[\Gamma_{n,n}(q_{||}, \omega)] - 1$ ($q_{||} = q_{||}^*$ for $n = n' = 1, 2$) occurs only within the small-value $q_{||} - \omega$ region due to the presence of the $\chi_{n,n}^{(0)}(q_{||}, \omega)$ interaction term in Eq. (7). In this case, the intrasubband-scattering resonance is determined by the peak of

$$\Gamma_{n,n}(q_{||}, \omega) = \left[1 - \left(\frac{Z^* e^2}{2\epsilon_0 \epsilon_d} \right)^2 \frac{2\mu^*}{\pi^2 \hbar^2} \chi_{n,n}^{(0)}(q_{||}, \omega) \times \left(\int_{-\mathcal{L}_0/2}^{\mathcal{L}_0/2} dz_0 \rho_d(z_0) |\bar{U}_{n,n}(q_{||}, z_0)|^2 \right) \right]^{-1}. \quad (9)$$

The strength of this intrasubband-scattering resonance decreases rapidly with increasing $q_{||}$ due to a reduced $|\bar{U}_{n,n}(q_{||}, z_0)|^2$ value from the suppressed long-range intrasubband scattering, as displayed in Fig. 2(d). For intersubband excitation with $n = 1$ and $n' = 2$, on the other hand,

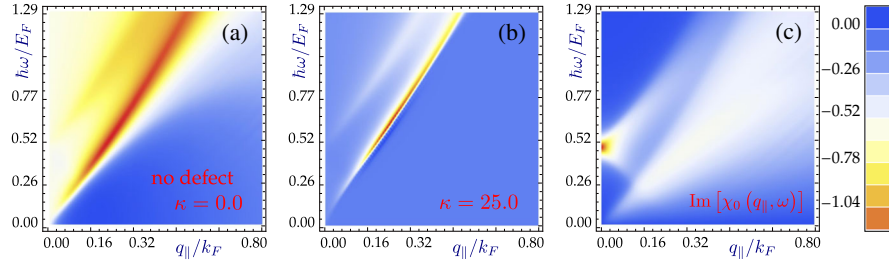


FIG. 4. Density plots for $1/\text{Re}\{\text{Det}[\vec{\epsilon}(q_{||}, \omega)]\}$ associated with two interlayer plasmon modes in (a) and (b), as well as for $\text{Im}\{\chi_{n,n}^{(0)}(q_{||}, \omega)\}$ [in units of $(2\mu^*/\hbar^2)$] related to two particle-hole continua in (c) with $n = 1, 2$, where the dimensionless dielectric-function matrix $\vec{\epsilon}(q_{||}, \omega)$ is defined in Eq. (4). In addition, $\kappa = 0$ in (a) and (c), while $\kappa = 25$ in (b). The other parameters used in the calculations are the same as those in Figs. 2 and 3.

the two $\Gamma_{1,2}$ terms with $q_{||}$ and $q_{||}^* = \sqrt{q_{||}^2 + 8\mu^* \varepsilon_{21}/\hbar^2}$ are coupled to each other, as can be verified by Eq. (7). As a result, the broad intersubband-scattering resonance shows up in Figs. 3(c) and 3(d), along with a sign switching in $\text{Re}[\Gamma_{1,2}(q_{||}, \omega)] - 1$ and a peak in $\text{Im}[\Gamma_{1,2}(q_{||}, \omega)]$. Furthermore, it is very important to notice that the broad intersubband-scattering resonance in Figs. 3(c) and 3(d), due to elastic coupling between the $q_{||}$ and $q_{||}^*$ electron states in the two subbands, is different from the sharp intersubband-plasmon resonance determined by $\chi_{1,2}^{(0)}(q_{||}, \omega)$ in Eq. (2).

The calculated $\Gamma_{n,n'}(q_{||}, \omega)$ in Fig. 3 is substituted into Eq. (4) to find the intralayer dielectric function modified by defects in the RPA. Graphically, the dispersion relations of intrasubband-plasmon modes appear as peaks in the density plot for the absolute value of the real part of $1/\text{Det}[\vec{\epsilon}(q_{||}, \omega)]$ within the $(\omega, q_{||})$ plane, where the dielectric-function matrix $\vec{\epsilon}(q_{||}, \omega)$ is defined in Eq. (4). In the absence of defects, from Figs. 4(a) and 4(c), we find two intrasubband-plasmon modes and two particle-hole continua (i.e., $\text{Im}\{\chi_{n,n}^{(0)}(q_{||}, \omega)\}$), correspondingly, for two occupied subbands in a quantum well. By further introducing defects to the quantum well in Fig. 4(b), the dispersion of the lower plasmon mode has been modified noticeably for small q_x values due to energy shifts from the contribution of $\text{Re}\{\Gamma_{n,n}(q_{||}, \omega)\}$, as shown in Fig. 3. Such a modification to the plasmon dispersion relation can have a nonlinear κ dependence for large κ values (or higher defect densities). The defect effect on the intersubband-plasmon mode is very weak and is not shown in Fig. 4.

By using Eq. (3) with this modified dielectric function, the resulting inverse dielectric function is further input into Eq. (1) to compute related changes in the screened partial polarization functions $\delta\chi_{n,n'}(q_{||}, \omega)$ of a single quantum well. For intrasubband excitations in Figs. 5(a) and 5(c), the defect-induced change $\delta\text{Im}[\chi_{1,1}(q_{||}, \omega)]$ displays a peak shift (sign switching) to a lower and lower value of ω with an increasing κ value. However, $\delta\text{Im}[\chi_{1,1}(q_{||}, \omega)]$ is

reduced significantly for a larger $q_{||}$ value due to weakened scattering interaction, as shown in Fig. 2(d). It is also interesting to notice that the depolarization shift of a plasmon peak ($\text{Im}[\chi_{1,1}(q_{||}, \omega)]$ vs $\text{Im}[\chi_{1,1}^{(0)}(q_{||}, \omega)]$) in the two insets (i1) and (i3) [with $\Gamma_{n,n'}(q_{||}, \omega) \equiv 1$] also increases with $q_{||}$, but it will not show up in $\delta\text{Im}[\chi_{1,1}(q_{||}, \omega)]$ for defect effects. This pure plasmon depolarization shift to a higher ω value is rooted in a many-body screening effect and is slightly reduced by defect scatterings. Similar features in $\delta\text{Im}[\chi_{1,2}(q_{||}, \omega)]$ can also be found in Fig. 5(d) for intersubband losses, but their magnitudes become much smaller due to very weak intersubband-scattering processes. In addition to the shift of this broad intrasubband-plasmon peak by defects, we also expect defect effects on a sharper intersubband-plasmon-loss peak (around $\hbar\omega \sim \varepsilon_{21}$) for a smaller $q_{||}$ value, as presented in the inset of Fig. 5(b), where nearly

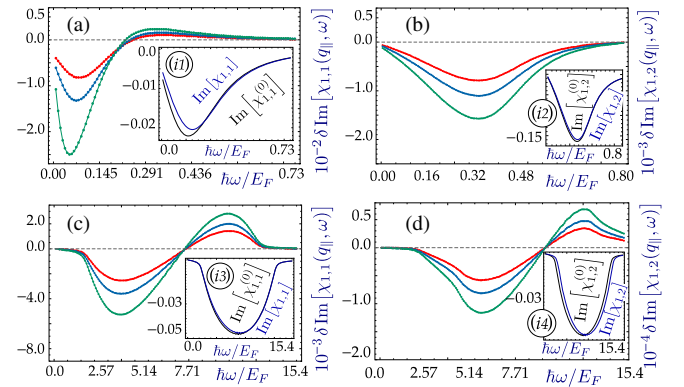


FIG. 5. (a),(c) $\delta\text{Im}[\chi_{1,1}(q_{||}, \omega)]$ and (b),(d) $\delta\text{Im}[\chi_{1,2}(q_{||}, \omega)]$ calculated from Eq. (1) as functions of $\hbar\omega/E_F$ for $\kappa = 5$ (red), 7 (blue), and 10 (green). Here, the parameters and units used for $\chi_{n,n'}^{(0)}(q_{||}, \omega)$ are the same as those in Figs. 2–4. Results are shown for (a),(b) $q_{||}/k_F = 0.1$ and (c),(d) 2.5. The inset of each panel compares the bare $\text{Im}[\chi_{n,n}^{(0)}(q_{||}, \omega)]$ value and the screened $\text{Im}[\chi_{n,n'}(q_{||}, \omega)]$ value under RPA in the absence of defects.

no shift of the intensive intersubband-plasmon peak is found.

B. Effects on energy loss of electron beams

In Sec. II A, we discuss the effects of defects on the intralayer partial polarization function $\chi_{n,n'}(q_{\parallel}, \omega)$. Here, we extend our study to the kinetic-energy loss of a ballistic electron beam by further taking into account the defect effects on the interlayer total polarization function. A full review on the excitation of collective modes, such as plasmons, in bulk materials, planar surfaces, and nanoparticles was reported in Ref. [35], and the light emission induced by the electrons has proven to be an excellent probe of plasmons, combining subnanometer resolution in the position of the electron beam with nanometer resolution in the emitted wavelength.

Let us assume that a semi-infinite semiconductor occupies the $z > 0$ half-space and consider a classical (heavy and slow) point charge Q_0 moving along a prescribed path $\mathbf{R}(t)$ in the air space ($z < 0$) outside the semiconductor region. In such a case, we find that the external potential Φ_{ext} associated with this moving charged particle in the quasistatic limit satisfies the instantaneous Poisson equation [36,37], i.e.,

$$\nabla_{\mathbf{r}}^2 \Phi_{\text{ext}}(\mathbf{r}, t|\mathbf{R}) = -\frac{Q_0}{\epsilon_0} \delta[\mathbf{r} - \mathbf{R}(t)], \quad (10)$$

where $\mathbf{R}(t) = \{\mathbf{R}_{\parallel}(t), Z(t)\}$ is the trajectory of the charged particle, and $\mathbf{r} = \{\mathbf{r}_{\parallel}, z\}$ is a position vector. The solution of Eq. (10) inside the region of $Z(t) < z < 0$ is found to be

$$\Phi_{\text{ext}}^<(\mathbf{r}, t|\mathbf{R}) = \int \frac{d^2 \mathbf{q}_{\parallel}}{(2\pi)^2} \int_{-\infty}^{\infty} \frac{d\omega}{2\pi} \phi_{\text{ext}}(\mathbf{q}_{\parallel}, \omega|\mathbf{R}) e^{i\mathbf{q}_{\parallel} \cdot \mathbf{r}_{\parallel} - i\omega t} e^{-q_{\parallel} z}, \quad (11)$$

where the Fourier-transformed external potential is calculated as

$$\phi_{\text{ext}}(\mathbf{q}_{\parallel}, \omega|\mathbf{R}) = -\frac{Q_0}{2\epsilon_0 q_{\parallel}} \mathcal{F}_0(\mathbf{q}_{\parallel}, \omega|\mathbf{R}), \quad (12)$$

and its structure factor is

$$\mathcal{F}_0(\mathbf{q}_{\parallel}, \omega|\mathbf{R}) = \int_{-\infty}^{\infty} dt' e^{q_{\parallel} Z(t')} e^{i\omega t' - i\mathbf{q}_{\parallel} \cdot \mathbf{R}_{\parallel}(t')}. \quad (13)$$

From a physics perspective, the existence of Φ_{ext} inside the semiconductor induces a potential Φ_{ind} outside the semiconductor (i.e., $z < 0$) due to the charge-density fluctuation, yielding

$$\Phi_{\text{ind}}^<(\mathbf{r}, t|\mathbf{R}) = -\int \frac{d^2 \mathbf{q}_{\parallel}}{(2\pi)^2} \int_{-\infty}^{\infty} \frac{d\omega}{2\pi} \phi_{\text{ext}}(\mathbf{q}_{\parallel}, \omega|\mathbf{R}) \times e^{i\mathbf{q}_{\parallel} \cdot \mathbf{r}_{\parallel} - i\omega t} \mathcal{S}(q_{\parallel}, \omega) e^{q_{\parallel} z}, \quad (14)$$

where $\mathcal{S}(q_{\parallel}, \omega)$ is the so-called surface-response function [11] determined later by matching the boundary condition. Within the semiconductor region ($0 \leq z \leq \mathcal{L}_0$), we write down similar expressions for the external $\Phi_{\text{ext}}^>$ and induced $\Phi_{\text{ind}}^>$ potentials, given by

$$\Phi_{\text{ext}}^>(\mathbf{r}, t|\mathbf{R}) = \int \frac{d^2 \mathbf{q}_{\parallel}}{(2\pi)^2} \int_{-\infty}^{\infty} \frac{d\omega}{2\pi} \phi_{\text{ext}}(\mathbf{q}_{\parallel}, \omega|\mathbf{R}) \times e^{i\mathbf{q}_{\parallel} \cdot \mathbf{r}_{\parallel} - i\omega t} \Phi_0^>(z|q_{\parallel}), \quad (15)$$

$$\Phi_{\text{ind}}^>(\mathbf{r}, t|\mathbf{R}) = -\int \frac{d^2 \mathbf{q}_{\parallel}}{(2\pi)^2} \int_{-\infty}^{\infty} \frac{d\omega}{2\pi} \phi_{\text{ext}}(\mathbf{q}_{\parallel}, \omega|\mathbf{R}) \times e^{i\mathbf{q}_{\parallel} \cdot \mathbf{r}_{\parallel} - i\omega t} \phi_{\text{ind}}^>(z|q_{\parallel}, \omega), \quad (16)$$

where $\Phi_0^>(z|q_{\parallel})$ is the bare external potential in the electrostatic limit ($q_{\parallel} c \gg \omega$) for a slab of semiconductor material of thickness \mathcal{L}_0 , $\Phi_0^>(0|q_{\parallel}) = 1 - g_{\text{slab}}(q_{\parallel})$, and $g_{\text{slab}}(q_{\parallel})$ is the surface-response function for a dielectric slab without doping electrons [11]. Since the total potential $\Phi_0^>(z|q_{\parallel}) + \phi_{\text{ind}}^>(z|q_{\parallel}, \omega)$ inside the semiconductor ($z > 0$) equals the screened external potential, we get $\phi_{\text{ind}}^>$ in Eq. (16) from [38]

$$\phi_{\text{ind}}^>(z|q_{\parallel}, \omega) = \int dz' [\epsilon^{-1}(z, z'|q_{\parallel}, \omega) - \delta(z - z')] \Phi_0^>(z'|q_{\parallel}). \quad (17)$$

In Eq. (17), the inverse dielectric function can be determined from

$$\epsilon^{-1}(z, z'|q_{\parallel}, \omega) = \delta(z - z') + \int dz'' V_c(z, z''|q_{\parallel}) \chi(z'', z'|q_{\parallel}, \omega), \quad (18)$$

where the interlayer Coulomb coupling $V_c(z, z'|q_{\parallel})$, including the image potentials, is calculated as [11]

$$V_c(z, z'|q_{\parallel}) = \frac{\beta_0(q_{\parallel}) e^2}{2\epsilon_0 \epsilon_d (q_{\parallel} + q_s)} [e^{-q_{\parallel} |z-z'|} + \alpha_0^2 e^{-2q_{\parallel} \mathcal{L}_0} e^{q_{\parallel} |z-z'|} + \alpha_0 e^{-q_{\parallel} |z+z'|} + \alpha_0 e^{-2q_{\parallel} \mathcal{L}_0} e^{q_{\parallel} |z+z'|}], \quad (19)$$

and $\alpha_0 = (\epsilon_d - 1)/(\epsilon_d + 1)$, $\beta_0(q_{\parallel}) = 1/[1 - \alpha_0^2 \exp(-2q_{\parallel} \mathcal{L}_0)]$.

For a multi-quantum-well system, the density-density-response function in Eq. (18) takes the form [36]

$$\chi(z, z'|q_{\parallel}, \omega) = \sum_{j, j'=0}^N \delta(z - ja) \tilde{\chi}_e(j, j'|q_{\parallel}, \omega) \delta(z' - j'a), \quad (20)$$

where a is the well separation, $\mathcal{L}_0 = Na$, and the screened polarization function $\tilde{\chi}_e(j, j'|q_{\parallel}, \omega)$ within the RPA can be obtained from the following self-consistent equations [36]:

$$\begin{aligned} \tilde{\chi}_e(j, j'|q_{\parallel}, \omega) &= \tilde{\chi}_j(q_{\parallel}, \omega) \delta_{j, j'} \\ &+ \tilde{\chi}_j(q_{\parallel}, \omega) \sum_{j''(\neq j)=0}^N V_c(ja, j''a|q_{\parallel}) \\ &\times \tilde{\chi}_e(j'', j'|q_{\parallel}, \omega). \end{aligned} \quad (21)$$

Here, the summation over j'' excludes the intralayer term with $j'' = j$, the integers $j = 0, 1, \dots, N$ labels different wells, and $\tilde{\chi}_j(q_{\parallel}, \omega) = \sum_{n \leq n'} \chi_{n, n'}(j, j|q_{\parallel}, \omega)$ is the total polarization function for the j th quantum well, as discussed in Sec. II A.

By combining Eqs. (17), (18), and (20), $\phi_{\text{ind}}^{\>}(z|q_{\parallel}, \omega)$ in Eq. (16) can be rewritten simply as

$$\phi_{\text{ind}}^{\>}(z|q_{\parallel}, \omega) = \sum_{j, j'=0}^N V_c(z, ja|q_{\parallel}) \tilde{\chi}_e(j, j'|q_{\parallel}, \omega) \Phi_0^{\>}(j'a|q_{\parallel}). \quad (22)$$

By matching the boundary condition for the total potential, i.e., $1 - \mathcal{S}(q_{\parallel}, \omega) = [1 - g_{\text{slab}}(q_{\parallel})] + \phi_{\text{ind}}^{\>}(0|q_{\parallel}, \omega)$ at the surface $z = 0$, we are able to find the surface-response function introduced in Eq. (14) from

$$\begin{aligned} \mathcal{S}(q_{\parallel}, \omega) &= g_{\text{slab}}(q_{\parallel}) \\ &- \sum_{j, j'=0}^N V_c(0, ja|q_{\parallel}) \tilde{\chi}_e(j, j'|q_{\parallel}, \omega) \Phi_0^{\>}(j'a|q_{\parallel}), \end{aligned} \quad (23)$$

where [36]

$$g_{\text{slab}}(q_{\parallel}) = 2\alpha_0 \beta_0(q_{\parallel}) e^{-q_{\parallel} Na} \sinh(q_{\parallel} Na), \quad (24)$$

and the external electrostatic potential in Eqs. (17) and (23) inside a slab of semiconductor ($0 \leq z \leq Na$) is found to be [36]

$$\begin{aligned} \Phi_0^{\>}(z|q_{\parallel}) &= \left[\frac{1 - g_{\text{slab}}(q_{\parallel})}{2} + \frac{g_{\text{slab}}(q_{\parallel})}{2\epsilon_d} \right] e^{-q_{\parallel} z} \\ &+ \left[\frac{1 - g_{\text{slab}}(q_{\parallel})}{2} - \frac{g_{\text{slab}}(q_{\parallel})}{2\epsilon_d} \right] e^{q_{\parallel} z}. \end{aligned} \quad (25)$$

The absorbed kinetic energy $\Delta E_{\text{abs}}\{\mathbf{R}\}$ of an electron beam can be calculated by integrating the Poynting vector

over the surface and over time in the air region, which leads to [38]

$$\begin{aligned} \Delta E_{\text{abs}}\{\mathbf{R}\} &= \epsilon_0 \int d^2 \mathbf{r}_{\parallel} \int_{-\infty}^{\infty} dt \text{Re} \left\{ [\Phi_{\text{tot}}^{\<}(\mathbf{r}, t|\mathbf{R})]^* \frac{\partial^2 \Phi_{\text{tot}}^{\<}(\mathbf{r}, t|\mathbf{R})}{\partial t \partial z} \right\} \Big|_{z=0}, \end{aligned} \quad (26)$$

where $\Phi_{\text{tot}}^{\<}(\mathbf{r}, t|\mathbf{R})$ is the total potential outside the semiconductor region ($z < 0$), calculated by combining Eqs. (11) and (14) and given by

$$\begin{aligned} \Phi_{\text{tot}}^{\<}(\mathbf{r}, t|\mathbf{R}) &= \int \frac{d^2 \mathbf{q}_{\parallel}}{(2\pi)^2} \int_{-\infty}^{\infty} \frac{d\omega}{2\pi} [e^{-q_{\parallel} z} - \mathcal{S}(q_{\parallel}, \omega) e^{q_{\parallel} z}] \\ &\times e^{i\mathbf{q}_{\parallel} \cdot \mathbf{r}_{\parallel} - i\omega t} \phi_{\text{ext}}(\mathbf{q}_{\parallel}, \omega|\mathbf{R}). \end{aligned} \quad (27)$$

Substituting this result into Eq. (26), we find

$$\begin{aligned} \Delta E_{\text{abs}}\{\mathbf{R}\} &= \frac{Q_0^2}{2\epsilon_0} \int \frac{d^2 \mathbf{q}_{\parallel}}{(2\pi)^2} \int_{-\infty}^{\infty} \frac{d\omega}{2\pi} \left(\frac{|\mathcal{F}_0(\mathbf{q}_{\parallel}, \omega|\mathbf{R})|^2 \omega}{q_{\parallel}} \right) \\ &\times \text{Im}\{\mathcal{S}(q_{\parallel}, \omega)\}, \end{aligned} \quad (28)$$

where $\text{Im}\{\mathcal{S}(q_{\parallel}, \omega)\}$ is the so-called loss function [11].

Specifically, for a charged particle moving parallel to the surface, we have $\mathbf{R}(t) = \{\mathbf{V}_{\parallel} t, Z_0\}$ and obtain

$$\begin{aligned} |\mathcal{F}_0(\mathbf{q}_{\parallel}, \omega|\mathbf{R})|^2 &= \lim_{\Delta T \rightarrow \infty} \left| \int_{-\Delta T/2}^{\Delta T/2} dt' e^{-q_{\parallel} Z_0} e^{i(\omega - \mathbf{q}_{\parallel} \cdot \mathbf{V}_{\parallel}) t'} \right|^2 \\ &= 2\pi \Delta T e^{-2q_{\parallel} |Z_0|} \delta(\omega - \mathbf{q}_{\parallel} \cdot \mathbf{V}_{\parallel}), \end{aligned} \quad (29)$$

which leads to the following power absorption for the parallel electron beam:

$$\begin{aligned} \frac{\Delta E_{\text{abs}}(V_{\parallel})}{\Delta T} &= \frac{Q_0^2}{2\epsilon_0} \int \frac{d^2 \mathbf{q}_{\parallel}}{(2\pi)^2} e^{-2q_{\parallel} |Z_0|} \left(\frac{\mathbf{q}_{\parallel} \cdot \mathbf{V}_{\parallel}}{q_{\parallel}} \right) \\ &\times \text{Im}[\mathcal{S}(q_{\parallel}, \mathbf{q}_{\parallel} \cdot \mathbf{V}_{\parallel})]. \end{aligned} \quad (30)$$

More interesting, if a charged particle moves away from the surface perpendicularly, we can write $\mathbf{R}(t) = \{0, Z_0 - V_{\perp} t\}$, with an impact parameter $|Z_0|$ ($Z_0 < 0$) and $0 \leq t \leq T_0$ for the damped particle, and obtain

$$\begin{aligned} |\mathcal{F}_0(\mathbf{q}_{\parallel}, \omega|\mathbf{R})|^2 &= \lim_{T_0 \rightarrow \infty} \left| \int_0^{T_0} dt' e^{-q_{\parallel} (|Z_0| + V_{\perp} t')} e^{i\omega t'} \right|^2 \\ &= \lim_{T_0 \rightarrow \infty} \left| \frac{e^{-q_{\parallel} |Z_0|}}{q_{\parallel} V_{\perp} - i\omega} [1 - e^{(q_{\parallel} V_{\perp} - i\omega) T_0}] \right|^2 \\ &= \frac{e^{-2q_{\parallel} |Z_0|}}{\omega^2 + q_{\parallel}^2 V_{\perp}^2}, \end{aligned} \quad (31)$$

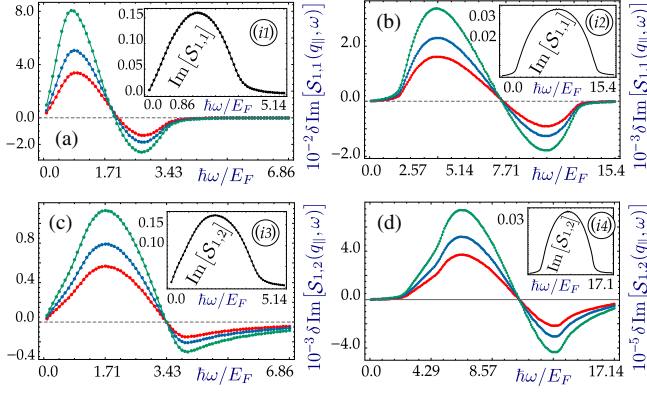


FIG. 6. Changes of loss function $\delta\text{Im}[\mathcal{S}_{n,n'}(q_{\parallel}, \omega)]$ calculated from Eq. (23) as functions of $\hbar\omega/E_F$ in the single quantum well for (a),(c) $q_{\parallel}/k_F = 1.0$ and (b),(d) $q_{\parallel}/k_F = 2.5$, with $\kappa = 5$ (red), 7 (blue), and 10 (green). The inset of each panel displays the dimensionless loss function $\text{Im}[\mathcal{S}_{n,n'}(q_{\parallel}, \omega)]$ in the absence of defects. Here, the parameters used in numerical calculations are the same as those in Figs. 2 and 3.

which yields the energy absorption for the perpendicular electron beam

$$\Delta E_{\text{abs}}(V_{\perp}) = \frac{Q_0^2}{2\epsilon_0} \int \frac{d^2\mathbf{q}_{\parallel}}{(2\pi)^2} \int \frac{d\omega}{2\pi} \left(\frac{\omega}{q_{\parallel}} \right) \frac{e^{-2q_{\parallel}|z_0|}}{\omega^2 + q_{\parallel}^2 V_{\perp}^2} \times \text{Im}\{\mathcal{S}(q_{\parallel}, \omega)\}. \quad (32)$$

In this case, the integral over ω with respect to the loss function $\text{Im}\{\mathcal{S}(q_{\parallel}, \omega)\}$ includes the damping contributions from both the particle-hole and collective excitation modes of electrons [39].

Multiple plasmon excitations in graphene materials by a single electron were predicted to give rise to a unique platform for exploring the bosonic quantum nature of these collective modes [40]. Such a technique not only opens a viable path toward multiple excitation of a single plasmon mode by a single electron but also reveals electron probes as an ideal tool for producing, detecting, and manipulating plasmons in graphene nanostructures.

For a single quantum well, the surface response function $\mathcal{S}(q_{\parallel}, \omega) = \sum_{n \leq n'} \mathcal{S}_{n,n'}(q_{\parallel}, \omega)$ can be obtained by setting $j = j' = 0$ in Eq. (23), and the total loss function is just $\text{Im}[\mathcal{S}(q_{\parallel}, \omega)] = \sum_{n \leq n'} \text{Im}[\mathcal{S}_{n,n'}(q_{\parallel}, \omega)]$. Here, the defect-induced change $\delta\text{Im}[\mathcal{S}_{n,n'}(q_{\parallel}, \omega)]$ directly relates to the imaginary part of the screened partial polarization function $\delta\text{Im}[\chi_{n,n'}(q_{\parallel}, \omega)]$ presented in Fig. 5. For $q_{\parallel}/k_F = 1.0$, we determine from Figs. 6(a) and 6(c) that $\delta\text{Im}[\mathcal{S}(q_{\parallel}, \omega)]$ is dominated by $\delta\text{Im}[\mathcal{S}_{1,1}(q_{\parallel}, \omega)]$ for a stronger intrasubband-scattering process, which increases with the defect-density scaling number κ . The sign switching reflects the shift of a loss peak [see the insets of Figs. 6(a) and 6(c)] to a lower value of ω . As q_{\parallel}/k_F is increased to 2.5 in Figs. 6(b) and 6(d), the resonant peak of $\text{Im}[\mathcal{S}(q_{\parallel}, \omega)]$ moves to a higher ω

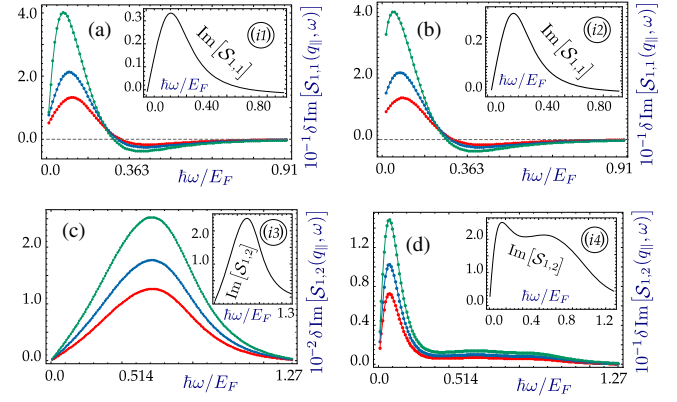


FIG. 7. Changes of loss function $\delta\text{Im}[\mathcal{S}_{n,n'}(q_{\parallel}, \omega)]$ calculated from Eq. (23) as functions of $\hbar\omega/E_F$ in single and multiple quantum wells at $q_{\parallel}/k_F = 0.1$ for (a),(c) $N_L = 1$ and (b),(d) $N_L = 3$, with $\kappa = 5$ (red), 7 (blue), and 10 (green). For defect distribution, we still use $\rho_d(z_0)/\kappa = \rho_1\Theta(-z_0 - L_W/2) + \rho_2\Theta(z_0 - L_W/2) + [\rho_0 + z_0(\Delta\rho/L_W)]\Theta(L_W/2 - |z_0|)$ for each quantum well and the two outer barriers, while $\rho_d(z_0)/\kappa$ is set to ρ_2 for the regions between the two adjacent quantum wells. The inset of each panel displays $\text{Im}[\mathcal{S}_{n,n'}(q_{\parallel}, \omega)]$ in the absence of defects. (b),(d) $a/L_W = 4$ and the other parameters used in the numerical calculations are the same as those found in Figs. 2 and 3.

value [comparing insets (i1) and (i2) to (i3) and (i4)]. However, the similar defect-related features as used in Figs. 6(a) and 6(c) are greatly weakened due to a dramatic reduction of scattering interactions, as shown in Fig. 2(d).

For a multi-quantum-well system, the interlayer Coulomb coupling $V_c(ja, j'a|q_{\parallel})$ in Eq. (21) will modify the intralayer total polarization function $\tilde{\chi}_j(q_{\parallel}, \omega)$, as well as the surface-response function in Eq. (23). From the comparison of single- and multi-quantum-well systems in Fig. 7, we find that the intersubband-plasmon loss $\text{Im}[\mathcal{S}_{1,2}(q_{\parallel}, \omega)]$ is strongly coupled to the intrasubband-plasmon loss $\text{Im}[\mathcal{S}_{1,1}(q_{\parallel}, \omega)]$ by interlayer Coulomb coupling, as shown in inset (i4). Here, the weaker $\text{Im}[\mathcal{S}_{1,1}(q_{\parallel}, \omega)]$ peak in inset (i2) is greatly enhanced by its sitting on the shoulder of a much stronger $\text{Im}[\mathcal{S}_{1,2}(q_{\parallel}, \omega)]$ peak in inset (i4), giving rise to a profile for the total $\text{Im}[\mathcal{S}(q_{\parallel}, \omega)]$ peak. As $q_{\parallel}/k_F = 0.1$, the defect-induced peak shift in $\delta\text{Im}[\mathcal{S}_{1,1}(q_{\parallel}, \omega)]$ to lower ω can be seen in Fig. 7(b), but not for $\delta\text{Im}[\mathcal{S}_{1,2}(q_{\parallel}, \omega)]$ in Fig. 7(d), except for a significant enhancement of the shoulder peak with an increasing κ value by interlayer Coulomb coupling. Moreover, by comparing Fig. 7(a) to Fig. 7(b), we find that both $\text{Im}[\mathcal{S}_{1,1}(q_{\parallel}, \omega)]$ and $\delta\text{Im}[\mathcal{S}_{1,1}(q_{\parallel}, \omega)]$ are dominated by the intralayer Coulomb coupling $\mathcal{V}_{m,m';n,n'}(q_{\parallel})$ given by Eq. (5).

C. Effects on loss of photons

In Sec. II B, the defect effects on the energy loss of electron beams in a multi-quantum-well system is

discussed. As a comparison, the defect effects on the loss of photons (or photon absorption) in the same system are investigated here. In this case, the absorption coefficients for both intrasubband and intersubband optical transitions of electrons can be calculated from [41]

$$\beta_{\text{abs}}(\omega) = \frac{\epsilon_d \omega}{n_r(\omega) c} \left[1 + \frac{1}{\exp(\hbar\omega/k_B T) - 1} \right] \times \text{Im}\{\alpha_L(\omega)\}, \quad (33)$$

where $\hbar\omega$ is the incident-photon energy and the dynamical refractive-index function $n_r(\omega)$ is

$$n_r(\omega) = \sqrt{\frac{\epsilon_d}{2} \left\{ 1 + \text{Re}\{\alpha_L(\omega)\} + \sqrt{[1 + \text{Re}\{\alpha_L(\omega)\}]^2 + [\text{Im}\{\alpha_L(\omega)\}]^2} \right\}^{1/2}}. \quad (34)$$

For intrasubband transitions with an optical probe field polarized parallel to the quantum-well planes, $\alpha_L(\omega)$ in Eqs. (33) and (34) is the Lorentz ratio, calculated as [12]

$$\alpha_L(\omega) = \alpha_L^{\parallel}(\omega) = - \left(\frac{2e^2}{\epsilon_0 \epsilon_d L_W} \right) \pi \mathcal{R}_0^2 \sum_{j=0}^N \int \frac{d^2 \mathbf{q}_{\parallel}}{(2\pi)^2} e^{-q_{\parallel}^2 \mathcal{R}_0^2 / 4} \mathcal{Q}_j^{\parallel}(q_{\parallel}, \omega), \quad (35)$$

where \mathcal{R}_0 is the radius of a normally incident Gaussian light beam, $N + 1$ is the total number of quantum wells in the system, and the optical-response function [42] $\mathcal{Q}_j^{\parallel}(q_{\parallel}, \omega)$ for the j th well is found to be

$$\mathcal{Q}_j^{\parallel}(q_{\parallel}, \omega) = \sum_n \tilde{\chi}_{n,n}(j, j|q_{\parallel}, \omega) \left(\frac{\hbar q_{\parallel}}{\mu^* \omega} \right)^2. \quad (36)$$

By including the coupling due to interlayer Coulomb interactions, the partial polarization function $\tilde{\chi}_{n,n}(j, j'; q_{\parallel}, \omega)$ introduced in Eq. (36) with $j = j'$ needs to be computed from the following self-consistent equations [36] (taking $n = n'$ and $j = j'$ afterwards), i.e.,

$$\begin{aligned} \tilde{\chi}_{n,n'}(j, j'|q_{\parallel}, \omega) &= \chi_{n,n'}(q_{\parallel}, \omega) \delta_{j,j'} \\ &+ \chi_{n,n'}(q_{\parallel}, \omega) \sum_{j''(\neq j)=0}^N V_c(ja, j''a|q_{\parallel}) \\ &\times \tilde{\chi}_{n,n'}(j'', j'|q_{\parallel}, \omega), \end{aligned} \quad (37)$$

where $\chi_{n,n'}(q_{\parallel}, \omega) \equiv \tilde{\chi}_{n,n'}(j, j|q_{\parallel}, \omega)$ and the interlayer Coulomb matrix elements $V_c(ja, j''a|q_{\parallel})$ are still found from Eq. (19). By further taking into account the coupling between different subbands in each quantum well, the screened partial polarization function $\chi_{n,n'}(q_{\parallel}, \omega)$ in Eq. (37) must be calculated from Eq. (1) after finding the inverse dielectric function from Eqs. (3) and (4).

On the other hand, for a spatially uniform optical probe field polarized perpendicular to the quantum-well planes, the Lorentz ratio $\alpha_L(\omega)$ in Eqs. (33) and (34) for intersubband transitions becomes [12]

$$\alpha_L(\omega) = \alpha_L^{\perp}(\omega) = - \frac{2e^2}{\epsilon_0 \epsilon_d L_W} \sum_{j=0}^N \mathcal{Q}_j^{\perp}(q_{\parallel} = 0, \omega), \quad (38)$$

where we assume $q_{\parallel}/k_F = \sqrt{\epsilon_d} \omega / k_F c \ll 1$, and k_F is the Fermi wave number of electrons in quantum wells. In this case, the optical-response function for the j th well in Eq. (38) takes the form [42]

$$\mathcal{Q}_j^{\perp}(q_{\parallel}, \omega) = \sum_{n < n'} \tilde{\chi}_{n,n'}(j, j|q_{\parallel}, \omega) \left| \int_{-\infty}^{\infty} dz \mathcal{F}_{n'}(z) z \mathcal{F}_n(z) \right|^2. \quad (39)$$

Moreover, the influence of interlayer Coulomb coupling on the intersubband partial polarization function $\tilde{\chi}_{n,n'}(j, j'|q_{\parallel}, \omega)$ should still be determined from Eq. (37) (setting $j = j'$ afterwards).

A periodic stack of graphene layers embedded within a dielectric bulk is expected to have the properties of a one-dimensional photonic crystal with stop bands at certain frequencies. As an incident electromagnetic wave is reflected from these stacked graphene layers, the tuning of the graphene Fermi energy or conductivity renders the possibility of controlling these stop bands, leading to a tunable spectral-selective mirror [43]. In addition, a transfer-matrix method is applied to explore optical reflection, transmission, and absorption in single-, double-, and multilayer graphene structures [44]. Both the total internal reflection in single-layer graphene and the thin-film interference effects in double-layer graphene are shown for increasing light absorption.

For intrasubband electron transitions induced by an optical field with a polarization parallel to the quantum-well plane, we present in Fig. 8(a) the defect modification to the absorption coefficient $\delta\beta_{\text{abs}}^{\parallel}(\omega)$ calculated with Eqs. (33) and (35). Here, the low-energy photon absorption peak in inset (i1) is attributed to the excitation of intrasubband plasmons, and this peak is shifted to an even lower ω value with an increasing κ value. On the other hand, for the intersubband transition of electrons under an optical field polarized perpendicular to the quantum-well plane, we display in Fig. 8(b) the defect changes in absorption coefficient $\delta\beta_{\text{abs}}^{\perp}(\omega)$ calculated from Eqs. (33) and (38). In this case, however, a high-energy and broad photon absorption peak in inset (i2) results from intrasubband-plasmon excitations, and no shift associated with this peak with κ is found.

As displayed in Figs. 8(a) and 8(b), reductions in proton-induced defects in both $\delta\beta_{\text{abs}}^{\parallel}(\omega)$ for intrasubband

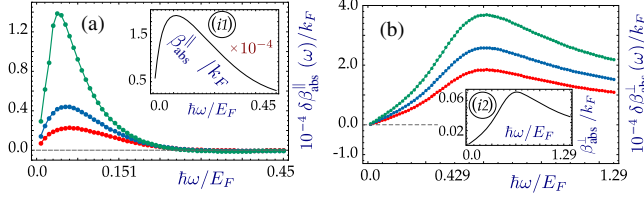


FIG. 8. Changes of intrasubband $\delta\beta_{\text{abs}}^{\parallel}(\omega)$ and intersubband $\delta\beta_{\text{abs}}^{\perp}(\omega)$ absorption coefficients (in units of k_F) calculated from Eqs. (35) and (38) as functions of $\hbar\omega/E_F$ for $N_L = 1$ and $\kappa = 5$ (red), 7 (blue), and 10 (green). The insets (i1) and (i2) of (a) and (b), respectively, present $\beta_{\text{abs}}^{\parallel}(\omega)$ and $\beta_{\text{abs}}^{\perp}(\omega)$ (in units of k_F) in the absence of defects. Here, $k_F\mathcal{R}_0 = 50$ and the other parameters used in the numerical calculations are the same as those found in Figs. 2 and 3.

absorption and $\delta\beta_{\text{abs}}^{\perp}(\omega)$ for intersubband absorption give rise to a decreased photoresponsivity [28,29] of quantum-well infrared detectors. As a consequence of this reduction, the lifetime of satellite onboard electronic and optoelectronic devices is shortened greatly. Therefore, the current theory can lead to a more realistic characterization of quantum-well photodetectors for not only high quantum efficiency and low dark current density [28,29] but also radiation tolerance or the ability to withstand the effects of the radiation they experience in a particular orbit.

III. ULTRAFAST POINT-DEFECT DYNAMICS

In Sec. II, we discuss only the effects of point defects on losses of electron energy and photons in a

multi-quantum-well system. In this section, we explore ultrafast dynamics for the production of Frenkel-pair defects and their follow-up reactions and diffusions in the same system. In this way, the spatial dependence of the one-dimensional distribution function $\rho_d(z)$ introduced in Eq. (7) for the defect-electron interaction can be extracted. It is known that Frenkel-pair production is followed subsequently by diffusion and reactions to reach defect stabilization through diffusion-induced recombination and reactions with residual defects in the system. Here, the diffusion of point defects is driven by forces other than the concentration gradient of defects, e.g., compressive stress near sinks. The reactions, on the other hand, are enabled by the presence of growth-induced dislocation loops at the two interfaces of a quantum well.

A. Defect diffusion-reaction equations

Let us start by considering an N -layered material structure in the z direction. Each material layer is characterized by the (bulk) irradiation parameters \mathcal{G}_0^j , \mathcal{R}^j , D^j , and $\Gamma^j(t)$, with layer labels $j = 1, 2, 3, \dots, N$, for production and recombination rates, diffusion coefficient, and bulk-sink annihilation, respectively. In modeling a mesoscopic-scale sample, the interface-sink strengths $[\kappa^j(t)]^2$, with $j = 1, 2, 3, \dots, N-1$, also need to be taken into account.

For a reaction-rate control system, we can write down the diffusion-reaction equations [1] for the concentrations of point vacancies and interstitial atoms as

$$\begin{aligned} \frac{\partial c_v^j(z, t)}{\partial t} - D_v^j \frac{\partial^2 c_v^j(z, t)}{\partial z^2} &= \mathcal{G}_0^j - \frac{\mathcal{B}_{iv}^j \Omega_j (D_i^j + D_v^j)}{(a_0^j)^2} c_i^j(z, t) c_v^j(z, t) \\ &- \sum_{\ell=4}^{\infty} \frac{\mathcal{B}_v^{j+1} D_v^{j+1} a_0^{j+1}}{1 - (\mathcal{B}_v^{j+1}/2\pi) \ln\{\pi [R_{vd}^{j+1}(\ell)]^2 \sigma_{\text{dl}}^{j+1}(\ell, t)\}} \sigma_{\text{dl}}^{j+1}(\ell, t) c_v^{j+1}(z, t) \delta(z - z_{j+1}) \\ &- \sum_{\ell=4}^{\infty} \frac{\mathcal{B}_v^j D_v^j a_0^j}{1 - (\mathcal{B}_v^j/2\pi) \ln\{\pi [R_{vd}^j(\ell)]^2 \sigma_{\text{dl}}^j(\ell, t)\}} \sigma_{\text{dl}}^j(\ell, t) c_v^j(z, t) \delta(z - z_j), \end{aligned} \quad (40)$$

$$\begin{aligned} \frac{\partial c_i^j(z, t)}{\partial t} - D_i^j \frac{\partial^2 c_i^j(z, t)}{\partial z^2} &= \mathcal{G}_0^j - \frac{\mathcal{B}_{iv}^j \Omega_j (D_i^j + D_v^j)}{(a_0^j)^2} c_i^j(z, t) c_v^j(z, t) \\ &- \sum_{\ell=4}^{\infty} \frac{\mathcal{B}_i^{j+1} D_i^{j+1} a_0^{j+1}}{1 - (\mathcal{B}_i^{j+1}/2\pi) \ln\{\pi [R_{id}^{j+1}(\ell)]^2 \sigma_{\text{dl}}^{j+1}(\ell, t)\}} \sigma_{\text{dl}}^{j+1}(\ell, t) c_i^{j+1}(z, t) \delta(z - z_{j+1}) \\ &- \sum_{\ell=4}^{\infty} \frac{\mathcal{B}_i^j D_i^j a_0^j}{1 - (\mathcal{B}_i^j/2\pi) \ln\{\pi [R_{id}^j(\ell)]^2 \sigma_{\text{dl}}^j(\ell, t)\}} \sigma_{\text{dl}}^j(\ell, t) c_i^j(z, t) \delta(z - z_j), \end{aligned} \quad (41)$$

where the small thermal-equilibrium concentration of point vacancies is neglected at low temperatures, \mathcal{B}_{iv}^j is the bias factor for recombinations [1], $\mathcal{B}_v^j \neq \mathcal{B}_i^j$ are the bias factors for vacancies (v) and interstitials (i), and D_v^j and D_i^j are the diffusion coefficients. The terms on the right-hand side of the equations correspond to diffusion sources and reactions, integer j is the layer index, integer ℓ indicates the number of interstitials enclosed within a planar dislocation loop [45], z_j and z_{j+1} represent the left and right interface positions of the j th layer, $c_v^j(z, t)$ and $c_i^j(z, t)$ are the concentrations of point vacancies and interstitials, and \mathcal{G}_0^j is the production rate for Frenkel pairs. Here, $\rho_d(z)$ can be obtained by multiplying the sample cross-section area with $c_v^j(z, t)$ and $c_i^j(z, t)$. In addition, in Eqs. (40) and (41), we use the facts that, in a reaction-rate control system, $\mathcal{R}^j \equiv \Gamma_{i,v}^j = \mathcal{B}_{iv}^j \Omega_j D_{i,v}^j / (a_0^j)^2$ for the vacancy-interstitial recombination rate, $\Gamma_{\{i,v\}d}^j(\ell, t) = [\kappa_{\{i,v\}d}^j(\ell, t)]^2 D_{\{i,v\}d}^j / \sigma_{dl}^j(\ell, t)$ is the rate for the interaction between defects and interface dislocation loops, and $[\kappa_{\{i,v\}d}^j(\ell, t)]^2 = \mathcal{B}_{\{i,v\}d}^j(\ell) \sigma_{dl}^j(\ell, t)$ for the dislocation loop-sink strength, where Ω_j is the atomic volume, a_0^j is the lattice constant, and $c_{FP}^j = \sqrt{\mathcal{G}_0^j (a_0^j)^2 / [\mathcal{B}_{iv}^j \Omega_j (D_i^j + D_v^j)]}$ is the initial number of Frenkel pairs. Furthermore, $\mathcal{B}_{\{i,v\}d}^j(\ell) \sim \mathcal{B}_{i,v}^j$ and $R_{\{i,v\}d}^j(\ell) \sim \ell a_0^j / 2\pi$ are the bias factors for the reactions and the capture radii of vacancy-dislocation loop (vd) and interstitial-dislocation loop (id), and, finally, $\sigma_{dl}^j(\ell, t)$ is the growth-strain-induced interface dislocation-loop (enclosing ℓ captured interstitial atoms) areal density.

The diffusion coefficients $D_{i,v}^j$ for point vacancies and interstitials can be calculated from [1]

$$D_{i,v}^j = \alpha^j (a_0^j)^2 \omega_D^j \exp\left(-\frac{E_{i,v}^j}{k_B T}\right), \quad (42)$$

where $E_{i,v}^j$ represents the migration energies for point vacancies and interstitials, α^j is determined by the diffusion mechanism and crystal symmetry, $\omega_D^j = (6\pi^2 / \Omega_j)^{1/3} v_s$ is the Debye frequency, and v_s is the sound velocity of the host semiconductor.

The interface dislocation-loop density $\sigma_{dl}^j(\ell, t)$ in Eqs. (40) and (41) can be found from the following reaction equation [1] (for $\ell \geq 4$), i.e.,

$$\begin{aligned} \frac{\partial \sigma_{dl}^j(\ell, t)}{\partial t} = & [\beta_v^j(\ell + 1, t) + \alpha_i^j(\ell + 1, t)] \sigma_{dl}^j(\ell + 1, t) \\ & + \beta_i^j(\ell - 1, t) \sigma_{dl}^j(\ell - 1, t) \\ & - [\beta_v^j(\ell, t) + \beta_i^j(\ell, t) + \alpha_i^j(\ell, t)] \sigma_{dl}^j(\ell, t), \end{aligned} \quad (43)$$

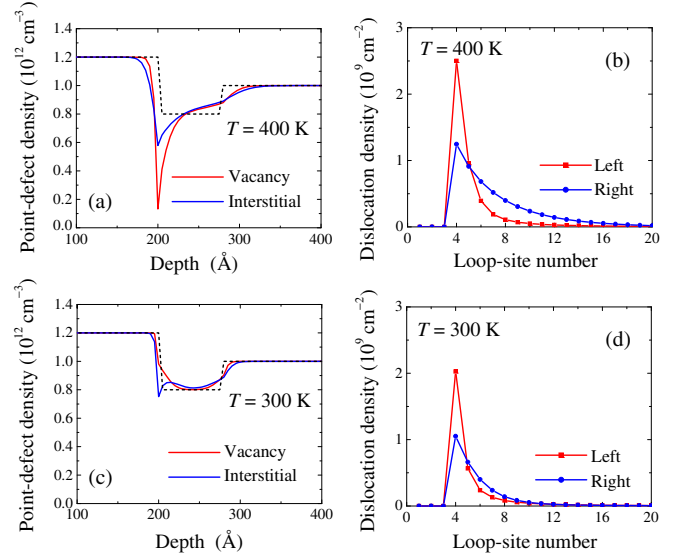


FIG. 9. Concentrations of (a),(c) point vacancies $c_v^j(z)$ and interstitials $c_i^j(z)$, and (b),(d) dislocation-loop densities $\sigma_{dl}^j(\ell)$ at two interfaces, in an AlAs-205 Å/InAs-75 Å/GaAs-255 Å single quantum well at (a),(b) $T = 400 \text{ K}$ and (c),(d) 300 K. Here, the \mathcal{G}_0^j values are 4.6, 0.9, and 2.1 in units of $10^{17} \text{ cm}^{-3} \text{ sec}^{-1}$ and the c_{FP}^j values are 1.2, 0.8, and 1.0 in units of 10^9 cm^{-3} for $j = 1, 2, 3$. In addition, the σ_0^j values are 2.0, 1.0 in units of 10^9 cm^{-2} for $j = 1, 2$. The values for other parameters, i.e., the bias factors, the absorption and emission rates, and the diffusion coefficients, are obtained from crystal symmetries [1] and by scaling melting temperatures with respect to SiC materials [46].

where $\sigma_{dl}^j(\ell, t = 0) = \sigma_0^j \delta_{\ell,4}$ and σ_0^j is the initial density for the smallest interface dislocation loops containing four interstitials, the absorption $[\beta_{i,v}^j(\ell, t)]$ and emission $[\alpha_i^j(\ell, t)]$ rates are given by [1]

$$\beta_{i,v}^j(\ell, t) = \ell a_0^j \mathcal{B}_{i,v}^j D_{i,v}^j c_{i,v}^j(z_j, t), \quad (44)$$

$$\alpha_i^j(\ell, t) = \ell a_0^j \mathcal{B}_i^j \left(\frac{D_i^j}{\Omega_j}\right) \exp\left[-\frac{E_{b,i}^j(\ell)}{k_B T}\right], \quad (45)$$

and $E_{b,v}^j(\ell)$ is the binding energy for a planar cluster of ℓ interstitials.

We show in Figs. 9(a) and 9(c) the steady-state spatial distributions for concentrations of point vacancies $c_v^j(z)$ and interstitials $c_i^j(z)$ in an AlAs/InAs/GaAs single-quantum-well system. We notice from Eqs. (40), (41), and (43) that both $c_v^j(z)$ and $c_i^j(z)$ in a steady state eventually become proportional to \mathcal{G}_0^j , although c_{FP}^j is initially proportional to $\sqrt{\mathcal{G}_0^j}$. In Fig. 9, the comparison of results at $T = 400 \text{ K}$ (upper panels) and 300 K (lower panels) are presented to demonstrate the diffusion of point vacancies into the well through both interfaces due to

thermally enhanced diffusion coefficients of vacancies. However, the interstitial concentration around the left interface is greatly depleted (there is a deep dip) at $T = 400$ K as a result of large absorptions by dislocation loops, although they still diffuse into the well through the right interface. In Figs. 9(b) and 9(d), we display results for steady-state distributions of dislocation-loop densities $\sigma_{dl}^j(\ell)$ ($\ell \geq 4$) as functions of the loop-site number, corresponding to the left ($j = 1$) and right ($j = 2$) interfaces at $T = 300$ and 400 K. Here, the increases of dislocation-loop densities ($\ell = 4$) at the left interface and the simultaneous swellings of dislocation loops ($\ell > 4$) at the right interface are found due to the enhanced reactions with point interstitials by their increased diffusion coefficients. Moreover, the defect diffusions occur mainly around interfaces between two adjacent layers or across the interfaces, and $c_v^j(z) \neq c_i^j(z)$ due to their different diffusion coefficients, although these two concentrations are initially identical.

If the penetration depth of protons is larger than the sample thickness, the overall distribution of defects for a multiple-quantum-well structure can be determined by repeating the single-well defect distribution along the growth direction. Therefore, our defect diffusion-reaction model for the AlAs/InAs/GaAs quantum well is adequate for the multi-quantum-well system.

B. Defect production by proton radiation

The diffusion-reaction equations presented in Sec. III A can be applied to find the spatial dependence of the one-dimensional distribution function $\rho_d(z)$ of the defects. However, the initial conditions of these equations require the production rate and the concentration of proton-produced Frenkel pairs. Therefore, we must study the production dynamics of point defects under proton irradiation with different kinetic energies, which connects the lab-measured defect effects (\propto number of point defects) to space-measured energy-dependent proton fluxes in a particular Earth orbit. For this purpose, an atomic-level molecular-dynamics simulation approach is employed, with help from a Tersoff potential fitted by parameters [46,47].

For a bulk material, the production rate per unit volume $\mathcal{G}_0(E_i)$ ($\text{sec}^{-1} \text{cm}^{-3}$) for the displacement atoms in a crystal lattice can be calculated from [1]

$$\mathcal{G}_0(E_i) = n_{\text{at}} \sigma_D(E_i) \mathcal{F}_0(E_i), \quad (46)$$

where E_i (MeV) is the incident proton kinetic energy, n_{at} (cm^{-3}) is the crystal atom volume density, $\mathcal{F}_0(E_i)$ ($\text{cm}^{-2} \text{sec}^{-1}$) is the incident energy-dependent proton flux, and $\sigma_D(E_i)$ (cm^2) is the energy-dependent displacement cross section.

Physically, the displacement cross section $\sigma_D(E_i)$ in Eq. (46) describes the probability for the displacement of

struck lattice atoms by incident protons; therefore, we can directly write

$$\sigma_D(E_i) = \int_{E_d}^{\varepsilon_{\text{max}}(E_i)} d\varepsilon_T \mathcal{Q}(\varepsilon_T) \sigma_C(E_i, \varepsilon_T) \mathcal{N}_{\text{MD}}(\varepsilon_T), \quad (47)$$

where $\sigma_C(E_i, \varepsilon_T)$ [$\text{cm}^2 (\text{keV})^{-1}$] is the differential energy transfer cross section by collision with the lattice, which measures the probability that an incident proton with kinetic energy E_i will transfer a recoil energy ε_T (keV) to a struck lattice atom, $\mathcal{N}_{\text{MD}}(\varepsilon_T)$ (no unit) represents the average number of displaced atoms produced by collision with the lattice, and E_d labels the energy threshold, i.e., the energy required to produce a stable Frenkel pair. In addition, $\varepsilon_{\text{max}}(E_i) = [4m_0M_0/(m_0 + M_0)^2]E_i$ is the upper limit for the recoil energy gained by the struck lattice atom, where M_0 refers to the mass of the lattice atoms and m_0 to the mass of the incident protons.

The function $\mathcal{Q}(\varepsilon_T)$ (dimensionless) introduced in Eq. (47) is the so-called Lindhard partition function and is written as [48–50]

$$\mathcal{Q}(\varepsilon_T) = \frac{1}{1 + \mathcal{K}_L g(\varepsilon_T/E_L)}, \quad (48)$$

where the Ziegler-Biersack-Littmark (ZBL) reduced-energy E_L is defined as

$$E_L = \left(\frac{m_0 + M_0}{M_0} \right) \frac{Z_1 Z_2 e^2}{4\pi\epsilon_0 a_u}, \quad (49)$$

while the reduced electronic energy-loss factor \mathcal{K}_L is

$$\mathcal{K}_L = \frac{Z_1^{2/3} Z_2^{1/2}}{12.6(Z_1^{2/3} + Z_2^{2/3})^{3/4}} \frac{[(1 + (M_0/m_0))]^{3/2}}{\sqrt{M_0/m_0}}, \quad (50)$$

$m_0 = 1.67 \times 10^{-27}$ kg is the proton mass, $a_u = 0.8853 a_B / (Z_1^{2/3} + Z_2^{2/3})^{1/2}$ is the ZBL universal screening length, $a_B = 4\pi\epsilon_0 \hbar^2 / m_e e^2 = 0.5292 \text{ \AA}$ is the Bohr radius, m_e is the free-electron mass, and the Lindhard function $g(x)$ is calculated as

$$g(x) = x + 0.40244x^{3/4} + 3.4008x^{1/6}. \quad (51)$$

In the current case, we set $Z_1 = 1$ (proton), $Z_2 = 31$ (Ga), or 33 (As) for the nuclear charge number of lattice atoms.

Moreover, the differential energy transfer cross section $\sigma_C(E_i, \varepsilon_T)$ [$\text{cm}^2 (\text{keV})^{-1}$] can be approximated as [50]

$$\sigma_C(E_i, \varepsilon_T) = -\frac{\pi a_u^2}{2} \alpha_s^2(E_i) \frac{h_0 \{[\tau(E_i, \varepsilon_T)]^{1/2}\}}{[\tau(E_i, \varepsilon_T)]^{3/2} \varepsilon_{\text{max}}(E_i)}, \quad (52)$$

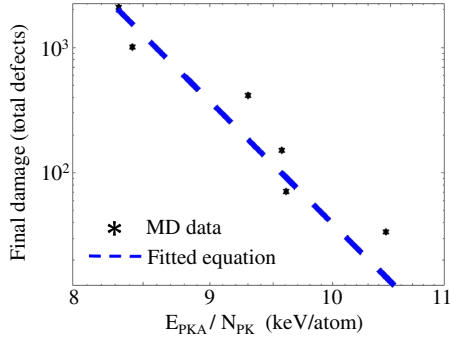


FIG. 10. Total number $\mathcal{N}_{\text{MD}}(\varepsilon_T)$ of defects in MD simulation as a function of the PKA energy $E_{\text{PKA}} \equiv \varepsilon_T$ scaled by the number N_{pk} of defects at the peak time in Fig. 11, where the formulas are $\mathcal{N}_{\text{MD}}(\varepsilon_T) = \mathcal{A}_0[\varepsilon_T(\text{keV})]^n$ and $N_{\text{pk}} = B_0[\varepsilon_T(\text{keV})]^\ell$, with parameters $\mathcal{A}_0 = 75.07$, $n = 1.11$, $B_0 = 64.15$, and $\ell = 1.04$ extracted from the fitting (the dashed curve). Here, the display is in logarithm scale with a straight-line dependence, while the fitting is done in linear scale with an exponential dependence. Here, the fitting result is presented on a logarithm scale with a straight-line-like dependence, while the fitting is done for a linear scale with an exponential dependence which requires a delicate fitting process.

where $\tau(E_i, \varepsilon_T) = \alpha_s^2(E_i)\varepsilon_T/\varepsilon_{\text{max}}(E_i)$ is the dimensionless collision parameter, and $\alpha_s(E_i) = E_i/E_L$ is the scaled ZBL reduced energy. The function $h_0(x)$ introduced in Eq. (52) is defined as

$$h_0(x) = \frac{\ln A(x)}{2B(x)} + \frac{ax}{2A(x)B(x)} - \frac{x \ln A(x)(1 + bcx^{c-1} + d/2x^{1/2})}{2B^2(x)}, \quad (53)$$

where $A(x) = 1 + ax$, $B(x) = x + bx^c + dx^{1/2}$, $a = 1.1383$, $b = 0.01321$, $c = 0.21226$, and $d = 0.19593$ are four parameters.

Finally, $\mathcal{N}_{\text{MD}}(\varepsilon_T)$ in Eq. (47) can be computed by using MD simulations. As shown in Fig. 10, the calculated $\mathcal{N}_{\text{MD}}(\varepsilon_T)$ can be fitted reasonably well by a simple power law, i.e., $\mathcal{N}_{\text{MD}}(\varepsilon_T) = \mathcal{A}_0[\varepsilon_T(\text{keV})]^n$ with proper fitting parameters \mathcal{A}_0 and n . Finally, by combining the results in Eqs. (46)–(52), for a given flux spectrum $\mathcal{F}_0(E_i)$, we get the production rate $\mathcal{G}_0(E_i)$ per unit volume as

$$\mathcal{G}_0(E_i) = -\frac{n_{\text{at}} \pi a_u^2 \mathcal{A}_0}{2} \left[\frac{\alpha_s^2(E_i) \mathcal{F}_0(E_i)}{\varepsilon_{\text{max}}(E_i)} \right] \times \int_{E_d}^{\varepsilon_{\text{max}}(E_i)} d\varepsilon_T \mathcal{Q}(\varepsilon_T) [\varepsilon_T(\text{keV})]^n \frac{h_0\{\tau(E_i, \varepsilon_T)\}^{1/2}}{[\tau(E_i, \varepsilon_T)]^{3/2}}, \quad (54)$$

which can be evaluated numerically once the fitting parameters \mathcal{A}_0 and n are obtained. Here, $\mathcal{G}_0(E_i)$ is related

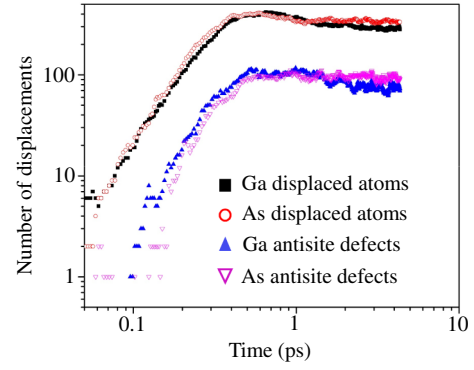


FIG. 11. The number of Ga and As displaced atoms and antisite defects as a function of time in a $\varepsilon_T = 10$ keV Ga-PKA cascade in GaAs, where the peak time of about 0.8 ps is found.

to the more familiar nonionizing energy loss [22] $\text{NIEL}(E_i)$ by $\mathcal{G}_0(E_i) = (\rho_{\text{at}}/n_{\text{at}})(0.4/E_d)\mathcal{F}_0(E_i)\text{NIEL}(E_i)$, with ρ_{at} being a crystal atom weight density [22]. Furthermore, the concentration $c_{\text{FP}}(E_i)$ for Frenkel-pair defects can be roughly estimated from $c_{\text{FP}}(E_i) = \mathcal{G}_0(E_i)(\tau_0 + \tau_i/2)$, where τ_i is the effective proton transit time through the sample, and $\tau_0 \sim 10$ ns, which is proportional to $1/\sqrt{\mathcal{F}_0(E_i)}$, is the time required to reach a steady state for generation of Frenkel-pair defects after the production has been balanced by the recombination.

We present in Fig. 11 the numerical results for a calculated number of lattice-atom displacements as a function of time after a Ga PKA has been introduced to a GaAs crystal with the recoil energy $\varepsilon_T = 10$ keV. From Fig. 11, we find that the number of lattice-atom displacements reaches a peak value N_{pk} at about $t = 0.8$ ps. After this peak time, only 13% of the displaced atoms recombine with vacancies, and most antisite defects are generated during the collisional phase. In addition, a steady state with $\varepsilon_T = 10$ keV has been reached for $t > 10$ ps, where As defects are slightly higher than Ga defects due to the smaller formation energy for As defects [23].

The numerical results for the number $\mathcal{N}_F(\varepsilon_T)$ of Ga and As displaced atoms and antisite defects as a function of recoil energy ε_T at $t = 10$ ps are displayed in Fig. 12, where the Norgett-Robinson-Torrens (NRT) result is given by $\mathcal{N}_F(\varepsilon_T) = N_{\text{NRT}}(\varepsilon_T) \equiv 0.8\varepsilon_T/2E_d$. It is clear from this figure that the number of defects at steady state is found to be much higher than that given by the NRT value. Moreover, nonlinear dependence on ε_T is limited only for low-energy PKA recoils.

In order to provide initial Frenkel-pair defect concentrations and its production rate, we show in Fig. 13 the numerical result of Eq. (54) for $\mathcal{G}_0(E_i)$. It is clear from this figure that there exists a peak for $\mathcal{G}_0(E_i)$ as a function of incident-proton kinetic energy due to competition between increasing the $\varepsilon_{\text{max}}(E_i)$ value and decreasing the $\sigma_C(E_i, \varepsilon_T)$ value at the same time.

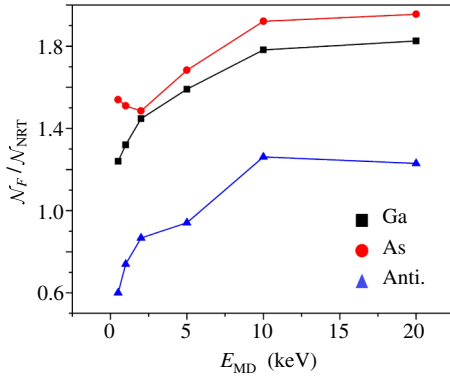


FIG. 12. The number $\mathcal{N}_F(\epsilon_T)$ of Ga and As displaced atoms and antisite defects as a function of recoil energy $E_{MD} \equiv \epsilon_T$ in MD simulation at $t = 10$ ps, where the NRT result is given by $\mathcal{N}_F(\epsilon_T) = 0.8\epsilon_T/2E_d$.

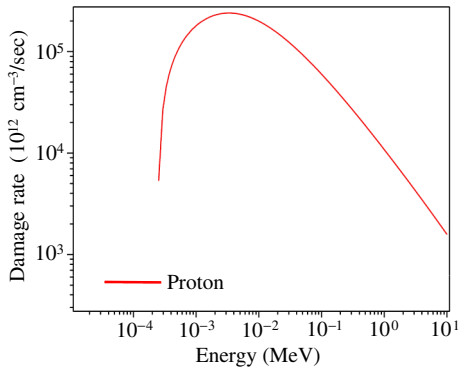


FIG. 13. Calculated defect production (or damage) rate $\mathcal{G}_0(E_i)$ per unit volume as a function of the incident-proton kinetic energy E_i . Here, the proton flux is assumed to be a constant $3.0 \times 10^{12} \text{ cm}^{-2} \text{ sec}^{-1}$.

IV. SUMMARY AND REMARKS

In conclusion, we investigate in this paper the effects of point defects on the loss of either electron kinetic energy or incident photons in a multi-quantum-well system. The influence of proton-radiation-produced defects is taken into account by applying the vertex correction to a bare polarization function of electrons in quantum wells within the ladder approximation, which goes beyond the usual second-order Born approximation. Both intralayer and interlayer dynamical screenings to the defect-electron interaction are also considered under the random-phase approximation. Furthermore, the defect effects on the electron-energy loss function, as well as on intrasubband and intersubband optical absorption, are shown and discussed.

To find the distribution function of point defects in a layered structure for calculations of defect effects, we apply the diffusion-reaction-equation method, where the reactions of point defects with the growth-induced dislocation

loops on interfaces of the multilayered system are included, and the increase and decrease of dislocation-loop density and point-defect concentrations are found at the same time due to the thermal enhancement of defect diffusion. In addition, the Frenkel-pair defect production rate and the initial concentration of Frenkel pairs are obtained from an atomic-level molecular-dynamics model after fitting the numerical results for Frenkel pairs as a function of energy of a primary knock on atom.

The defect-effect, diffusion-reaction, and molecular-dynamics models presented in this paper can be combined with a space-weather-forecast model [20,21] which predicts spatiotemporal fluxes and particle velocity distributions. In addition, the atomic-level molecular-dynamics model employed in this paper is based on a fitted short- and long-range interaction among all atoms from extensive calculations using the first-principle density-functional theory for an individually considered material. With this combination of theories, the predicted irradiation conditions for particular satellite orbits allow electronic and optoelectronic devices to be specifically designed for operation in space with radiation-hardening considerations [17] (such as self-healing and mitigation). This approach will effectively extend the lifetime of satellite onboard electronic and optoelectronic devices in nonbenign orbits and will greatly reduce the cost. The theory in this paper can be applied to space-based sensing and imaging, and it can lead to a more realistic characterization of quantum-well photodetectors for not only high quantum efficiency and low dark current density but also radiation tolerance or mitigation of the effects of the radiation.

ACKNOWLEDGMENTS

This material is based upon work supported by the Air Force Office of Scientific Research (AFOSR). We would also like to thank Dr. Paul D. LeVan and Dr. Sanjay Krishna for the helpful discussions.

-
- [1] G. S. Was, *Fundamentals of Radiation Materials Science: Metals and Alloys* (Springer-Verlag, Berlin, 2007).
 - [2] P. Sigmund, *Particle Penetration and Radiation Effects* (Springer-Verlag, Berlin, 2006).
 - [3] K. Nordlund, J. Peltola, J. Nord, J. Keinonen, and R. S. Averback, Defect clustering during ion irradiation of GaAs: Insight from molecular dynamics simulations, *J. Appl. Phys.* **90**, 1710 (2001).
 - [4] R. Devanathan, W. J. Weber, and F. Gao, Atomic scale simulation of defect production in irradiated 3C-SiC, *J. Appl. Phys.* **90**, 2303 (2001).
 - [5] M. Posselt, F. Gao, and D. Zwicker, Atomistic study of the migration of di- and tri-interstitials in silicon, *Phys. Rev. B* **71**, 245202 (2005).

- [6] F. Gao and W. J. Weber, Recovery of close Frenkel pairs produced by low energy recoils in SiC, *J. Appl. Phys.* **94**, 4348 (2003).
- [7] F. Gao, H. Xiao, X. Zu, M. Posselt, and W. J. Weber, Defect-Enhanced Charge Transfer by Ion-Solid Interactions in SiC using Large-Scale *Ab Initio* Molecular Dynamics Simulations, *Phys. Rev. Lett.* **103**, 027405 (2009).
- [8] Z. Rong, F. Gao, and W. J. Weber, Monte Carlo simulations of defect recovery within a 10 keV collision cascade in 3C-SiC, *J. Appl. Phys.* **102**, 103508 (2007).
- [9] L. A. Maksimov and A. I. Ryazanov, Kinetic equation for vacancy pores. Pore lattice as a dissipative structure, stable under irradiation conditions, *Sov. Phys. JETP* **52**, 1170 (1981).
- [10] S. I. Golubov, A. V. Barashev, and R. E. Stoller, in *Comprehensive Nuclear Materials*, edited by R. Konings, R. Stoller, T. Allen, and S. Yamanaka (Elsevier, Amsterdam, 2012), Chap. 13, pp. 357–391.
- [11] G. Gumbs and D. H. Huang, *Properties of Interacting Low-Dimensional Systems* (Wiley-VCH Verlag GmbH, Weinheim, 2011).
- [12] D. H. Huang and M. O. Manasreh, Intersubband transitions in strained $\text{In}_{0.07}\text{Ga}_{0.93}\text{As}/\text{Al}_{0.40}\text{Ga}_{0.60}\text{As}$ multiple quantum wells and their application to a two-colors photodetector, *Phys. Rev. B* **54**, 5620 (1996).
- [13] T. Ando, A. B. Fowler, and F. Stern, Electronic properties of two-dimensional systems, *Rev. Mod. Phys.* **54**, 437 (1982).
- [14] G. Gumbs, D. H. Huang, Y. Yin, H. Qiang, D. Yan, F. H. Pollak, and T. F. Noble, Many-body effects in the electro-modulation spectra of modulation-doped quantum wells: Theory and experiment, *Phys. Rev. B* **48**, 18328 (1993).
- [15] A. Hallén, D. Fenyö, B. U. R. Sundqvist, R. E. Johnson, and B. G. Svensson, The influence of ion flux on defect production in MeV proton irradiated silicon, *J. Appl. Phys.* **70**, 3025 (1991).
- [16] N. V. Doan and G. Martin, Elimination of irradiation point defects in crystalline solids: Sink strengths, *Phys. Rev. B* **67**, 134107 (2003).
- [17] D. H. Huang, F. Gao, D. A. Cardimona, C. P. Morath, and V. M. Cowan, Multi-timescale theory for radiation degradation of electronic and optoelectronic devices, *Am. J. Space Sci.* **3**, 3 (2015).
- [18] J. E. Hubbs, P. W. Marshall, C. J. Marshall, M. E. Gramer, D. Maestas, J. P. Garcia, G. A. Dole, and A. A. Anderson, Lateral diffusion length changes in HgCdTe detectors in a proton environment, *IEEE Trans. Nucl. Sci.* **54**, 2435 (2007).
- [19] C. Claeys and E. Simoen, *Radiation Effects in Advanced Semiconductor Materials and Devices* (Springer, New York, 2002).
- [20] M. Moldwin, *An Introduction to Space Weather* (Cambridge University Press, New York, 2008).
- [21] D. L. Cooke and I. Katz, Ionization-induced instability in an electron-collecting sheath, *J. Spacecr. Rockets*, **25**, 132 (1988).
- [22] F. Gao, N. J. Chen, E. Hernandez-Rivera, D. H. Huang, and P. D. LeVan, Displacement damage as revealed by computer simulations and effective non-ionizing energy loss in GaAs, *J. Appl. Phys.* **121**, 095104 (2017).
- [23] N. J. Chen, S. Gray, E. Hernandez-Rivera, D. H. Huang, P. D. LeVan, and F. Gao, Computational simulation of threshold displacement energies of GaAs, *J. Mater. Res.* **32**, 1555 (2017).
- [24] V. M. Cowan, C. P. Morath, J. E. Hubbs, S. Myers, E. Plis, and S. Krishna, Radiation tolerance characterization of dual band InAs/GaSb type-II strain-layer superlattice pBp detectors using 63 MeV protons, *Appl. Phys. Lett.* **101**, 251108 (2012).
- [25] C. P. Morath, V. M. Cowan, L. A. Treider, G. Jenkins, and J. E. Hubbs, Proton irradiation effects on the performance of III-V-based, unipolar barrier infrared detectors, *IEEE Trans. Nucl. Sci.* **62**, 512 (2015).
- [26] B. F. Levine, Quantum-well infrared photodetectors, *J. Appl. Phys.* **74**, R1 (1993).
- [27] A. Rogalski, Quantum well photoconductors in infrared detector technology, *J. Appl. Phys.* **93**, 4355 (2003).
- [28] D. H. Huang and D. A. Cardimona, Physics of non-adiabatic transport and field-domain effect in quantum-well infrared photodetectors, *Infrared Phys. Technol.* **44**, 487 (2003).
- [29] D. H. Huang, C. Morath, D. A. Cardimona, and A. Singh, Thermal hysteresis loop, dynamical breakdown, and emission-current spike in quantum-well photodetectors, *J. Appl. Phys.* **90**, 6032 (2001).
- [30] D. H. Huang and S.-X. Zhou, Theoretical investigation of collective excitations in HgTe-CdTe superlattices. I. Intrasubband excitation, *Phys. Rev. B* **38**, 13061 (1988).
- [31] D. H. Huang and S.-X. Zhou, Theoretical investigation of collective excitations in HgTe-CdTe superlattices. II. Intersubband excitation and effects of magnetic field and electron-phonon coupling, *Phys. Rev. B* **38**, 13069 (1988).
- [32] D. H. Huang, G. Gumbs, and N. J. M. Horing, Magneto-optical absorption in a one-dimensional array of narrow antiwires, *Phys. Rev. B* **49**, 11463 (1994).
- [33] D. H. Huang and M. O. Manasreh, Effects of the screened exchange interaction on the tunneling and Landau gaps in double quantum wells, *Phys. Rev. B* **54**, 2044 (1996).
- [34] D. H. Huang, P. M. Alsing, T. Apostolova, and D. A. Cardimona, Coupled energy-drift and force-balance equations for high-field hot-carrier transport, *Phys. Rev. B* **71**, 195205 (2005).
- [35] F. J. García de Abajo, Optical excitations in electron microscopy, *Rev. Mod. Phys.* **82**, 209 (2010).
- [36] G. Gumbs, Inelastic electron scattering from the surfaces of semiconductor multilayers: Study of subband structure within the quantum well, *Phys. Rev. B* **39**, 5186 (1989).
- [37] G. Gumbs and N. J. M. Horing, Plasma losses by charged particles in thin films: Effects of spatial dispersion, phonons, and magnetic field, *Phys. Rev. B* **43**, 2119 (1991).
- [38] B. N. J. Persson and E. Zaremba, Electron-hole pair production at metal surfaces, *Phys. Rev. B* **31**, 1863 (1985).
- [39] A. Iurov, G. Gumbs, D. H. Huang, and V. Silkin, Plasmon dissipation in gapped-graphene open systems at finite temperatures, *Phys. Rev. B* **93**, 035404 (2016).
- [40] F. J. García de Abajo, Multiple excitation of confined graphene plasmons by single free electrons, *ACS Nano* **7**, 11409 (2013).
- [41] G. Gumbs, D. H. Huang, and D. N. Talwar, Doublet structure in the absorption coefficient between tunneling

- split intersubband transitions in double quantum wells, *Phys. Rev. B* **53**, 15436 (1996).
- [42] D. H. Huang, C. Rhodes, P. M. Alsing, and D. A. Cardimona, Effects of longitudinal field on transmitted near field in doped semi-infinite semiconductors with a surface conducting sheet, *J. Appl. Phys.* **100**, 113711 (2006).
- [43] Yu. V. Bludov, N. M. R. Peres, and M. I. Vasilevskiy, Unusual reflection of electromagnetic radiation from a stack of graphene layers at oblique incidence, *J. Opt.* **15**, 114004 (2013).
- [44] T. Zhan, X. Shi, Y. Dai, X. Liu, and J. Zi, Transfer matrix method for optics in graphene layers, *J. Phys. Condens. Matter* **25**, 215301 (2013).
- [45] R. Bullough, M. R. Hayns, and C. H. Woo, The sink strength of dislocation loops and their growth in irradiated materials, *J. Nucl. Mater.* **84**, 93 (1979).
- [46] F. Gao and W. J. Weber, Atomic-scale simulation of 50 keV Si displacement cascades in β -SiC, *Phys. Rev. B* **63**, 054101 (2000).
- [47] J. Tersoff, New empirical approach for the structure and energy of covalent systems, *Phys. Rev. B* **37**, 6991 (1988).
- [48] S. R. Messenger, E. A. Burke, M. A. Xapsos, G. P. Summers, R. J. Walters, I. Jun, and T. Jordan, NIEL for heavy ions: An analytical approach, *IEEE Trans. Nucl. Sci.* **50**, 1919 (2003).
- [49] J. F. Ziegler, J. P. Biersack, and U. Littmark, *The Stopping and Range of Ions in Solids*, Vol. I (Pergamon Press, New York, 1985).
- [50] M. Nastasi, J. W. Mayer, and J. K. Hirvonen, *Ion-Solid Interactions, Fundamentals and Applications*, Cambridge Solid State Science Series (Cambridge University Press, New York, 2004).